이학박사 학위논문

Origins and evolution of Interplanetary Dust Particles

행성간 티끌의 기원과 진화

2018년 2월

서울대학교 대학원

물리·천문학부 천문학전공

양 홍 규

Origins and evolution of Interplanetary Dust Particles

행성간 티끌의 기원과 진화

지도교수 Masateru Ishiguro

이 논문을 이학박사 학위논문으로 제출함

2017년 10월

서울대학교 대학원

물리·천문학부 천문학전공

양 홍 규

양 홍 규의 이학박사 학위논문을 인준함

2017년 12월

위 원 장 이 형목

부 위 원 장 이시구로 마사테루

위 원 김 웅 태

위 원 천 석 민

위 원 표 정 현

Abstract

This dissertation aims to investigate the origins and evolution of Interplanetary Dust Particle (IDP) cloud complex. It is considered that there should be recent or continuous origins for the IDPs, and yet previous estimations about fractional contribution of given source populations (asteroids, comet, etc.) to the IDP cloud complex vary according to methodologies. Since it is likely that some critical factors may not be considered in the previous models, we tried to investigate this problem with additional consideration. We obtained the optical zodiacal light brightness around the anti-solar direction, and derived the mean albedo of IDPs as 0.06 ± 0.01. We compared the measured albedo and spectral gradient of the zodiacal light with those of potential parent bodies in the solar system. From Bayesian inference, we found that $> 90\%$ of the IDPs are originated from comets (or their spectral analogs, D-type asteroids).

Next, we investigated the orbital evolution of cometary dust particles, taking account of additional factors of non-compact dust shape and mutual collisions among IDPs. Both factors were not incorporated with planetary gravity and solar radiation in the previous models. We produced the dust size frequency distribution (SFD) measured around the Earth's orbit assuming the initial SFD measured at the comae of comets (1P/Halley, 67P/Churyumov-Gerasimenko, 73P/Schwassmann-Wachmann 3, and 81P/Wild 2).

Other new discoveries include followings: The spectrum of IDPs are similar to those of chondritic porous micrometeorites discovered in the Earth's stratosphere; There would be little chance for mutual collisions between IDPs if they are dominated by cometary particles; Dust particles from Jupiter-Family Comets are usully kicked out to the outer solar system through close encounters with Jupiter, if it is larger than 100

μm; Total mass supply rate to the IDPs cloud complex from Jupiter-Family Comets and Encke-Type comets is about 30–50 tons s^{-1}.

keywords : Interplanetary dust particles; zodiacal light; methods – numerical; dust particles – dynamical evolution and stability; comets – general; minor planets, asteroids – general

Student number : 2012-30112

Contents

List of Figures

List of Tables

Chapter 1

General Introduction

1.1 Interplanetary Dust Particles (IDPs)

Interplanetary Dust Particles (IDPs) are solid materials distributed in interplanetary space around the Sun. Because we observe the IDPs from the inside of the dust cloud (IDPs cloud complex), it is difficult to grasp the entire structure of IDPs cloud complex through an observation. Accordingly, we have to infer the structure from the complex's diverse manifestations. When IDPs encounter with the Earth, they ablate in the Earth's atmosphere, to be observed as meteors (Loehle et al. 2017; Bloxam & Campbell-Brown 2017; Plane et al. 2018); otherwise they are collected in the Earth's stratosphere (Bradley 2003) and the Antarctic ice (Noguchi et al. 2015). When IDPs collided with the impact detectors on the spacecrafts of the *Pioneer* (Dikarev & Grün 2002), *Galileo* (Krüger et al. 1998), *Ulysses* (Krüger et al. 2006), *Cassini* (Altobelli et al. 2007), and *New Horizons* (Poppe et al. 2010), impact records far from the Earth's orbit were obtained. The zodiacal light, which is scattered sunlight (Kwon et al. 2004) or thermal radiation (Kelsall et al. 1998; Pyo et al. 2010; Kondo et al. 2016) from IDPs can be observed from the Earth or spacecrafts.

The dust density distribution of IDPs cloud complex was mainly studied through zodiacal light observations. Kelsall et al. (1998) established a model IDPs cloud complex as a mixture of six components (smooth cloud, three pairs of dust bands, solar ring, and trailing blob, see Figure 1.1). Each component is approximated by mathematical formula, which describes dust number densities as a function of position for the six components. This model is successful in explaining zodiacal light brightness observed from the Earth-bound orbit as it is. The model has been upgraded with better accuracy by Pyo et al. (2010) and Kondo et al. (2016).

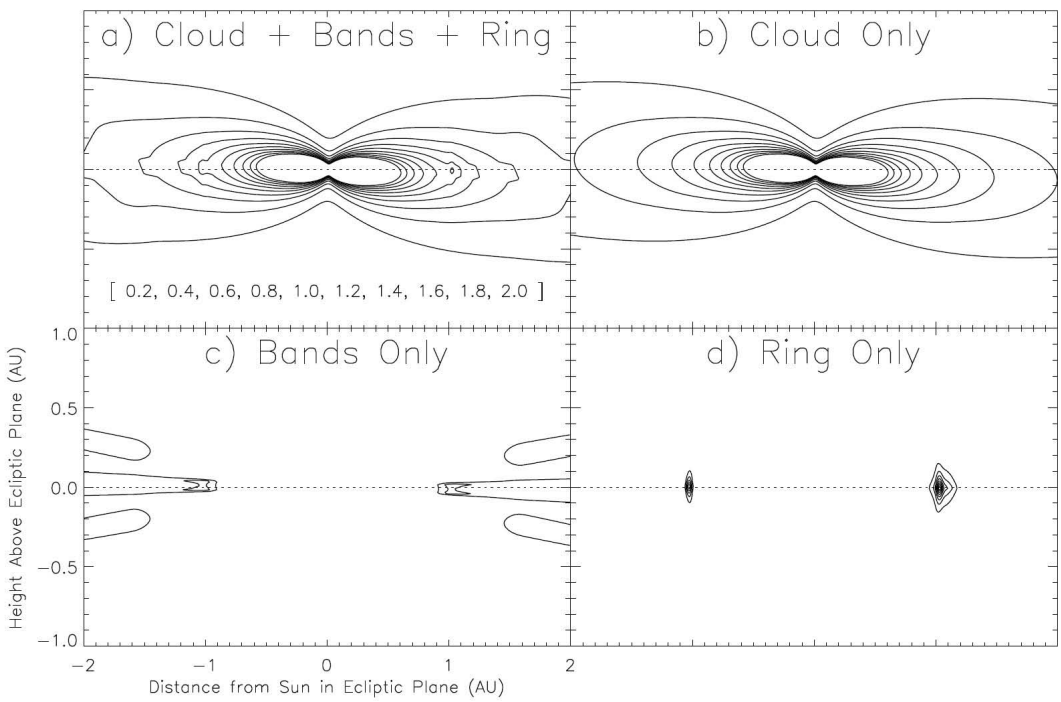

Figure 1.1. Contours of the IDPs cloud number density model components. Cross-sectional slice perpenticular to the ecliptic plane were described. The density contour levels for (a) and (b) are listed in bracket at the bottom of (a), and contour levels for (c) and (d) are a factor of 8 smaller than those for (a) and (b). (from Kelsall et al. 1998)

IDPs cloud complex models of previous paragraph explained relative number density distribution of the complex, but did not describe dust velocity, orbit, and size. Divine (1993) provided a model which simultaneously produces zodiacal light brightness distribution and impact flux records on spacecrafts, considering a mixture of five dust populations. Each of the populations described dust number density as a function of orbital elements and size. Later, this model was improved by Dikarev et al. (2005), including newer observations and implementing basic concern about the dynamics.

1.2 Origins of IDPs

Although the spatial distribution of IDPs cloud complex has been investigated by a variety of approaches as shown above, the origins of the IDPs cloud complex cannot be revealed sufficiently by the current IDPs distribution. Since the orbits of IDPs are exposed to chaotic gravitational perturbations by the planets, their past orbits should differ from their current ones. Moreover, even when there is no planetary perturbation (although it is an unrealistic assumption), the orbits of IDPs keep changing because of Poynting-Robertson photon drag (hereafter P–R drag) (Burns et al. 1979; Klačka et al. 2014; Burns et al. 2014). Due to the P–R drag, IDPs continuously migrate spirally into the Sun. Therefore, even IDPs which were originally on stable orbits cannot survive in the interplanetary spaces for a long time. Without planetary perturbations, IDPs are supposed to fall to the Sun within timescales shorter than 10 million years through the P–R drag (Mann et al. 2006, for $\lesssim$ 1 mm particles). This timescale is three orders of magnitude shorter than the age of the solar system. Therefore, it is obvious that recent or continuous dust sources are required to sustain current IDPs cloud complex. In this section, we will check the possible sources one by one, and summarize previous researches about the origins of IDPs.

The Sun cannot be the main source of the IDPs except the solar corona region. Because of P–R drag, dust particles are falling to the Sun, not moving from the Sun, for sizes larger than $\sim$ few μm. Planets are too massive for dust particles to escape from, in ordinary situations. It was suggested that Kuiper Belt Objects (hereafter KBOs) generate dust particles through collisions with interstellar dust particles (Yamamoto & Mukai 1998). However, dynamical studies of KBOs dust particles (Kuchner & Stark 2010; Vitense et al. 2012; Poppe 2016) revealed that their contribution to the zodiacal light brightness and meteor flux should be negligible. Kuchner & Stark (2010) thus pointed out that KBOs dust particles are concentrated out of Jovian orbit, suggesting that KBOs dust particles are not connected with the zodiacal light, because of the fact

that the zodiacal light brightness became negligible out of 3.3 au from the Sun from a spacecraft observation (Toller 1981). Poppe (2016) estimated that KBOs dust particle's contribution would be about 1% of that of Jupiter Family Comets (hereafter JFC) around the Earth's orbit (Figure 1.2) through an investigation of the dynamical evolution. These two works differ in details, but concur that KBOs dust particles are not contributing in the inner solar system.

As we suggested the impacts between KBOs and interstellar dust particles in the previous paragraph, it is thought that flux of interstellar dust particles passes through the solar system (Mann 2010; Sterken et al. 2015). The *Galileo* (Krüger et al. 2001), *Ulysses* (Krüger et al. 2015), and *STEREO* (Belheouane et al. 2012) detected high-speed ($\sim$26 km s^{-1} in the out of the solar system), small (diameter smaller than 10 μm) dust particles come from a fixed direction. With the speed and direction, these dust particles are regarded as interstellar origin. However, those particle's small size and short remaining time within the solar system raise questions about their contribution to the IDPs cloud complex. Reach et al. (2003) declined any meaningful interstellar dust contribution to the 10 μm emission in the zodiacal light spectrum. Because of the result, Nesvorný et al. (2010) assumed that interstellar dust particles are smaller than 1 μm, and ignored their contribution to the zodiacal light. On the other side, more recent impact records suggested existence of few–10 μm interstellar dust particles (Mann et al. 2014), and Rowan-Robinson & May (2013) insisted 7.5 % of interstellar dust contribution to the zodiacal light assuming existence of 4 μm interstellar dust particles.

and Mann et al. (2014) discussed possible interstellar dust contribution to the zodiacal light, while Reach et al. (2003) declined meaningful interstellar dust contribution to the zodiacal light and later works like Nesvorný et al. (2010) ignored interstellar dust because of Reach et al. (2003).

Dust ejection from asteroids was thoroughly studied since the discovery of zodiacal dust bands (Low et al. 1984; Kelsall et al. 1998; Ishiguro et al. 1999). The zodiacal dust bands are brightness enhancement in the zodiacal light around the ecliptic latitudes associated with asteroidal families. Dermott et al. (1984) conjectured that mutual collisions between asteroids were ongoing throughout the asteroidal belt, and consequently the collision rates were high enough to produce the detectable bands structures within the large asteroidal families. Therefore, they figured a large amount of asteroidal dust ejection out of dust bands (Durda & Dermott 1997; Jorda et al. 2000, $\sim$25% of total IDPs, additional 10–30% in the bands), and expected continuous dust ejection. On the contrary, another asteroidal collision model which connected a single catastrophic collision event to a pair of zodiacal dust bands was suggested (Sykes & Greenberg 1986;

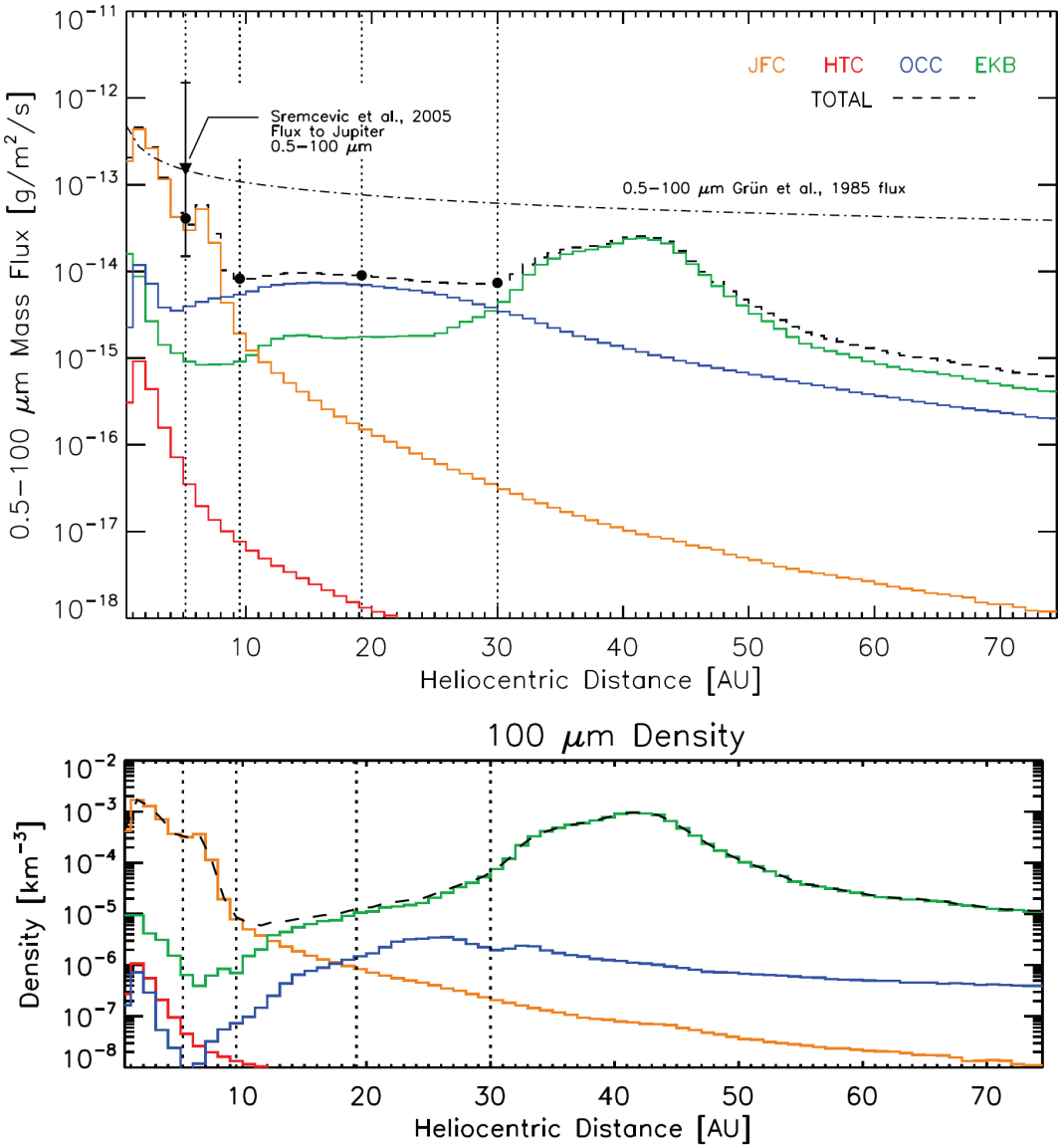

Figure 1.2. Mass flux for 0.5–100 μm dust particles and 100 μm particles number density as a function of heliocentric distance. Different colors mean different sources of dust particles; Jupiter Family Comets (JFCs), Halley Type Comets (HTCs), Oort Cloud Comets (OCCs), and Kuiper Belt Objects (EKB, we refer it as KBOs in the body). (from Poppe 2016)

Farley et al. 2006; Nesvorný et al. 2006, 2008). According to this model, a catastrophic breakup of an asteroid happened once a few millions of years, and a small collisional asteroidal family and a pair of dust bands should be simultaneously generated from the collisional fragments. This model explains observed zodiacal light brightness distribution better than the continuous collisional model. In the catastrophic breakup model, an ongoing asteroidal dust ejection out of dust bands structure is not necessary, and dust bands particles may comprise 5–10% of total IDPs cloud complex (Nesvorný et al. 2006, 2008). It is important to notice that the latter model gains widespread support on the basis of recent discoveries of young asteroidal families (Nesvorný et al. 2006, 2008).

More recently, the observational studies were conducted for the asteroidal dust ejection events which are not related to the dust bands. Ishiguro et al. (2011) and Kim et al. (2017) discovered impact-triggered activities from asteroids. The total contribution of such events to the total IDPs cloud complex is not clear in this moment, however, Jewitt et al. (2013) made crude estimate of < 3 % of contribution. It is also suggested that an asteroid may rotationally disintegrate and eject dust particles through the breakup (Moreno et al. 2014; Jewitt et al. 2017). Furthermore, a dozen of active asteroids have been discovered (Jewitt et al. 2015). Active asteroids are objects which have orbits like ordinary asteroidal one, but show dust ejection activity like comets. Generally, we do know neither the origins of nuclei of active asteroids nor the cause of their activity, although some mechanisms such as ice sublimation has been suggested. In this sense, out of dust bands, asteroidal dust supply to the IDPs cloud complex is not sure both in fractional contribution and absolute amount.

Comets are obviously ejecting dust particles through cometary activity. However, the total amount of dust ejection from comets is not easy to be estimated. The amounts of dust ejection from hundreds of comets are not studied well. Some studies about orbital and collisional evolutions of cometary dust particles are not enough to explain details of observations (further explanations in next section). Lastly, it is not clear how much fraction of cometary dust particles are ejected through ordinary cometary activity of sublimation. From time to time, cometary nuclei experience fragmentation (Fernández 2009; Ishiguro et al. 2009; Jewitt et al. 2016) or outburst (Ishiguro et al. 2014, 2016a,b). The fractional contributions to the IDPs cloud complex between ordinary ice-sublimation activities, fragmentations, and outbursts are not determined quantitatively until now.

As explained in this section, the plausible sources of IDPs consist of comets, asteroids, and interstellar dust particles. The fractional contribution from each possible source population is not determined well even among recent investigations. The cometary contribution is expected to 40–70 % (Ipatov et al. 2008, from Doppler shift of zodiacal light

Fraunhofer line), ∼70 % (Rowan-Robinson & May 2013, from kinematical matching of zodiacal light latitudinal profile), more than 90 % (Nesvorný et al. 2010, from dynamical matching of zodiacal light latitudinal profile). The asteroidal contribution is expected between 30–50 % (Ipatov et al. 2008), ∼22 % (Rowan-Robinson & May 2013), less than 10 % (Nesvorný et al. 2010). The contribution of interstellar particles is ignored (Ipatov et al. 2008; Nesvorný et al. 2010) or expected to ∼ 7.5 % of IDPs (Rowan-Robinson & May 2013). Furthermore, one recent study mentioned that UV spectrum of zodiacal light is similar with C-type asteroids (Kawara et al. 2017), implying that C–type asteroids are dominant sources of IDPs cloud complex.

1.3 Evolution of IDPs

The orbits of IDPs evolve by means of several factors. The gravitational perturbations from planets are always affecting the orbits of dust particles. The perturbations include secular perturbations, resonance perturbations, and close encounters. The secular perturbations can be estimated by analytical methods in most cases (Milani & Knezevic 1990; Murray & Dermott 1999). Whereas the consequences of the resonance perturbations were numerically investigated (Milani & Knezevic 1994; Dermott et al. 1994), the close encounters were not discussed for the dust particles. However, the dust particles ejected from JFCs are injected into unstable orbits which tend to encounter with the Jupiter in close distances, therefore a careful treatment of the close encounters is required. Because planetary perturbations, especially the close encounters are basically chaotic, the consequences of the perturbations may dramatically change when other perturbations are coexist with planetary perturbations. One of such factors is radiation effects from the Sun. Unlike larger asteroids, IDPs are influenced by radiation pressure, P–R drag and solar wind drag (Burns et al. 1979; Klačka et al. 2014; Burns et al. 2014). Because of radiation pressure from the Sun, particles are susceptible to the repulsive force, and it works as if the gravitational force from the Sun decreases. As explained in previous section, P–R and solar wind drag continuously decrease a dust particle's semi-major axis and eccentricity. Because the strengths of those radiation forces are primarily proportional to particle cross section (not particle mass), the orbital evolutions of dust particles also depend on particle size, the mass density and shape, even between the particles with same position and velocity. Dust particles which are smaller in size, lower in density, with non-spherical shape are more strongly influenced by the radiation forces and solar wind drag. Under these situations, as noted above, the chaotic nature of planetary perturbation may differentiate between the orbital evolution of dust particles

on the basis of particle size, density, and shape.

Therefore, the size-frequency distribution (hereafter SFD) of IDPs may change with time, at different location of the solar system place, depending on source populations. The measured SFD of IDPs around the Earth's orbit (Grün et al. 1985) differs from those obtained around the location of the dust sources (Fulle et al. 1995; Green et al. 2004, 2007; Vaubaillon & Reach 2010; Rotundi et al. 2015; Fulle et al. 2015; Hilchenbach et al. 2016; Fulle et al. 2016a; Bentley et al. 2016; Agarwal et al. 2016; Mannel et al. 2016; Merouane et al. 2016). The difference was not explained by dynamical studies, and the explanation will answer questions about IDPs origins and evolutionary tracks.

In addition to the orbital evolutions caused by the gravitational and radiational accelerations, catastrophic mutual collisions between IDPs may change the evolutionary consequences of the IDPs. Previously, collisional lifetime of IDPs was studied for particles in fixed circular orbits without dynamical evolution (Dohnanyi 1978; Grün et al. 1985; Steel & Elford 1986). It is concluded that IDPs larger than 200 μm disappear from the interplanetary spaces through the collisional breakup. The results were considered in previous dynamical researches (Wiegert et al. 2009; Nesvorný et al. 2011; Pokorný et al. 2014), even for the particles on evolving eccentric orbits ignoring the original assumption (i.e., the fixed circular orbits). However, recently, Soja et al. (2016) calculated collisional probability of IDPs on fixed eccentric orbits, and reported that the collisional lifetime would be longer than that of fixed circular orbits in Grün et al. (1985). Therefore, to answer questions of previous paragraphs, a comprehensive research on the collisional probabilities for IDPs on evolving eccentric orbits should be required.

1.4 Purpose of the dissertation

This dissertation aims to investigate the origins and evolution of the IDPs cloud complex. Previously, the origins of IDPs cloud complex were studied through the spatial distribution of zodiacal light brightness (Nesvorný et al. 2010; Rowan-Robinson & May 2013) or Doppler shift of zodiacal light Fraunhofer line (Ipatov et al. 2008). However, the results of those research did not concur each other as explained in section 1.2. In this dissertation, we will investigate the origins of IDPs cloud complex in an independent method. We will compare the optical properties (spectral gradient and geometrical albedo) of the zodiacal light with those of solar system minor bodies. This part will be explained in chapter 2.

As explained in section 1.3, the evolution of IDPs are not fully explained, especially for eccentric cometary particles. We will explain two unexplained questions about IDPs

evolution. We simultaneously explain the SFD of IDPs obtained at different places in the solar system; calculate the collisional probabilities of dust particles in time-evolving eccentric orbits. We address this question through dynamical simulation of IDPs. We implement the planetary perturbation, solar radiation, and mutual collision in the dynamical simulation. Effects of the particle source populations, mass density, and shape are considered (chapter 3).

Chapter 2

Origins of IDPs through Optical Properties of Zodiacal Light

[1]

2.1 Introduction to chapter 2

The purpose of this chapter is to investigate the origin of IDPs while taking into account the optical properties of zodiacal light in comparison with minor bodies in the solar system, such as comets and asteroids. An enormous number of IDPs are distributed in interplanetary space. They are observable through scattered sunlight in the optical wavelength (zodiacal light) and through thermal radiation in the mid- and far- infrared wavelengths (zodiacal emission). The IDP cloud, occasionally referred to as the zodiacal cloud, erodes on a time scale of 10^3–10^7 years (depending on the size and orbit, $< 1/100$ of the age of the solar system) due to Poynting–Robertson drag, mutual collisions among the IDPs, and planetary perturbations (Gor'kavyi et al. 1997; Dikarev et al. 2001; Mann et al. 2006). The mass-loss rate around the Earth's orbit was estimated to be $\approx 10^3$ kg s^{-1} (Grün et al. 1985; Mann & Czechowski 2005, and later, updated by ourselves (see chapte 3)). It is therefore, natural to suppose that ongoing dust production, through mechanisms such as impacts or ice sublimation, is compensating for the erosion of the zodiacal cloud.

The origins of IDPs have been studied through the spatial distribution of the zodiacal light. Early research which attempted to explain the dust band structures implied a large

[1]Most contents in this chapter was published in (Yang & Ishiguro 2015). Section 2.2.1 and the related contents were rewritten based on another paper, Ishiguro et al. (2013), in which the author of this PhD dissertation played a significant contribution on the data reduction of the paper.

contribution from the asteroidal origin IDPs (see, e.g. Dermott et al. (1996)). Later, Hahn et al. (2002) compared the surface brightness distribution of zodiacal light, taken with the *Clementine* spacecraft on-board camera, to the inclination distributions of comets and asteroids, and suggested that a significant fraction of dust particles at 1 au are of cometary origin. Nesvorný et al. (2010) further performed a numerical simulation for dust particles ejected from six different orbital groups (i.e., asteroid families, main belt asteroids, Jupiter family comets (JFCs), dormant JFCs, Halley-type comets, and Oort cloud comets), and compared the brightness distribution of the modeled zodiacal emission with that observed by an infrared space telescope. They suggested that 85%–95% of IDPs observable as zodiacal emission are originated from JFCs.

Although these recent studies on the brightness distribution favor cometary origin, little is known about the origin of IDPs in terms of their optical properties. In this chapter, we derived the geometric albedo of IDPs by comparing the brightness of the Gegenschein (a part of the zodiacal light enhanced by backward scattering enhancement) to the infrared model (Kelsall et al. 1998). Using the albedo value along with spectral gradients of the zodiacal light (Leinert et al. 1998), we considered the origin of IDPs through a comparison of the optical properties of the zodiacal light with those of the potential parent bodies, and present a discussion based on previous studies.

2.2 Methodology for the optical analysis

The SFD of IDPs was studied through lunar microcrater counting and in situ flux measurements (Grün et al. 1985; Divine 1993). These studies suggested that the effective cross-section of IDPs around the Earth's orbit is dominated by large (10–100 μm) particles. In that case, the particle sizes are significantly larger than the optical wavelength. Accordingly, we can assume that the optical properties of IDPs are similar to those of big objects, such as comets and asteroids. Thus, in the following discussion in chapter 2, we postulate the albedo (A) and the spectral gradient (S') of the IDPs based on those of the potential dust sources.

2.2.1 Albedo and spectral gradient of zodiacal light

The albedo of IDPs has been measured using several methods. Hanner (1980) compared the zodiacal light brightness to the IDP model derived from the lunar microcrater records. Lumme & Bowell (1985) derived the albedo value of IDPs, which can explain the polarization distribution of zodiacal light. Dumont & Levasseur-Regourd (1988) compared the optical and infrared brightness at a solar elongation of 90° to derive the albedo.

Despite these efforts, there is no consistent result for the albedo value. In this work, we attempted to measure the geometric albedo of IDPs by comparing the optical and infrared (Kelsall et al. 1998) zodiacal light flux at the anti-solar point.

The Wide–field Imager of Zodiacal light with ARray Detector (WIZARD, Figure 2.1) was developed by a team of Kobe University and University of Tokyo, to obtain high–resolution wide–field image of optical zodiacal light (Ishiguro et al. 2003). The instrument covers $46^\circ \times 92^\circ$ field of view with $1.'4$ pixel resolution at the wavelength range of 440–520 nm. I contributed the data reduction of images taken by the research team. The detailed description about the instruments, data acquisition, and data reduction are written in Yang (2012).

From the Gegenschein images around the anti-solar point (Figure 2.2), we discovered sharp brightness peak at the exact anti-solar point (Figure 2.3). Even though the brightness enhancement pattern around the anti-solar point changed seasonally, the position of brightness peak was always at the anti-solar point. This behavior of the sharp brightness peak coincides with the previous study in Buffington et al. (2009). The strong anti-solar point peak is interpreted as the opposition effect (coherent backscattering and/or shadow-hiding effect), which happens when lights are scattered to the backward direction from the Sun.

By definition, the geometric albedo is a ratio of the backward scattering intensity of a given objects respect to the intensity of Lambertian disk with the same cross-section (Hanner et al. 1981). We derived the total cross-section of IDPs at the anti-solar direction from a model (Kelsall et al. 1998), which was created based on the infrared observation of the zodiacal emission. Using the cross-section and measured anti-solar zodiacal light brightness in optical wavelength, we deduced that the geometric albedo of the zodiacal light to 0.07 ± 0.01. After subtracting weak fine-scale structures of asteroidal dust bands, the albedo of the smooth zodiacal light component is 0.06 ± 0.01 (Ishiguro et al. 2013, I participated in the project as the second author). We adopt this albedo value of 0.06 ± 0.01 below.

Small bodies in the solar system generally show linear spectra in a range of 4500–7500 Å. It is useful to express the spectral index using the normalized reflectivity gradient, S' [% 10^{-3} Å]:

$$S' = \frac{1}{\bar{S}} \frac{dS}{d\lambda}, \tag{2.1}$$

where S is the reflectance, defined as the flux density of an object divided by the flux density of the Sun at the wavelength λ, and $\bar{S}$ and $dS/d\lambda$ denote the average reflectance and spectral gradient in the wavelength range, respectively. The spectrum of zodiacal

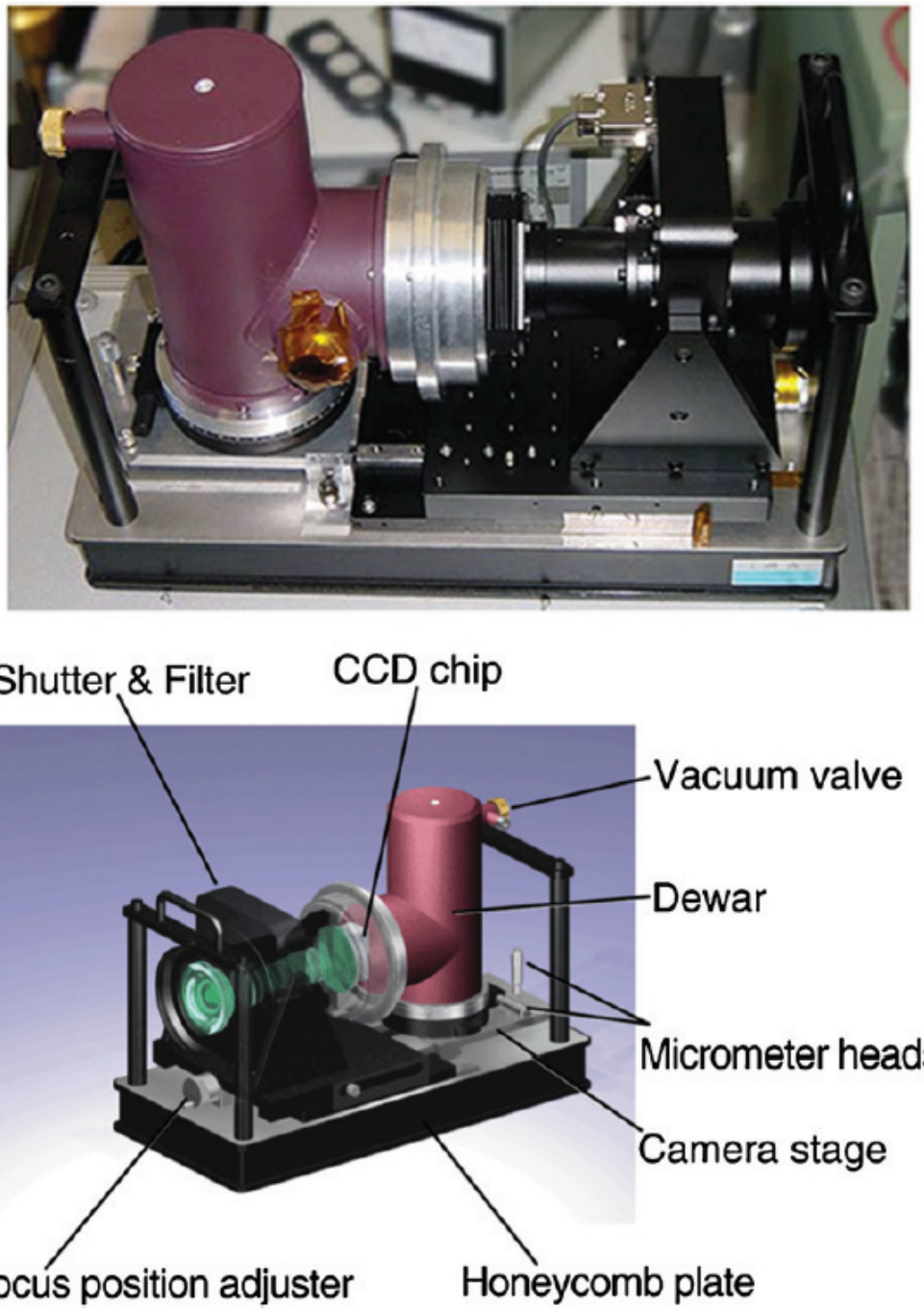

Figure 2.1. Photograph (top) and schematic view (bottom) of WIZARD. The system was mounted on an equatorial mount during the data acquisition at Mauna Kea (from Ishiguro et al. 2013). The top figure is provided by Professor Masateru Ishiguro and the bottom by Doctor Fumihiko Usui (Kobe University)

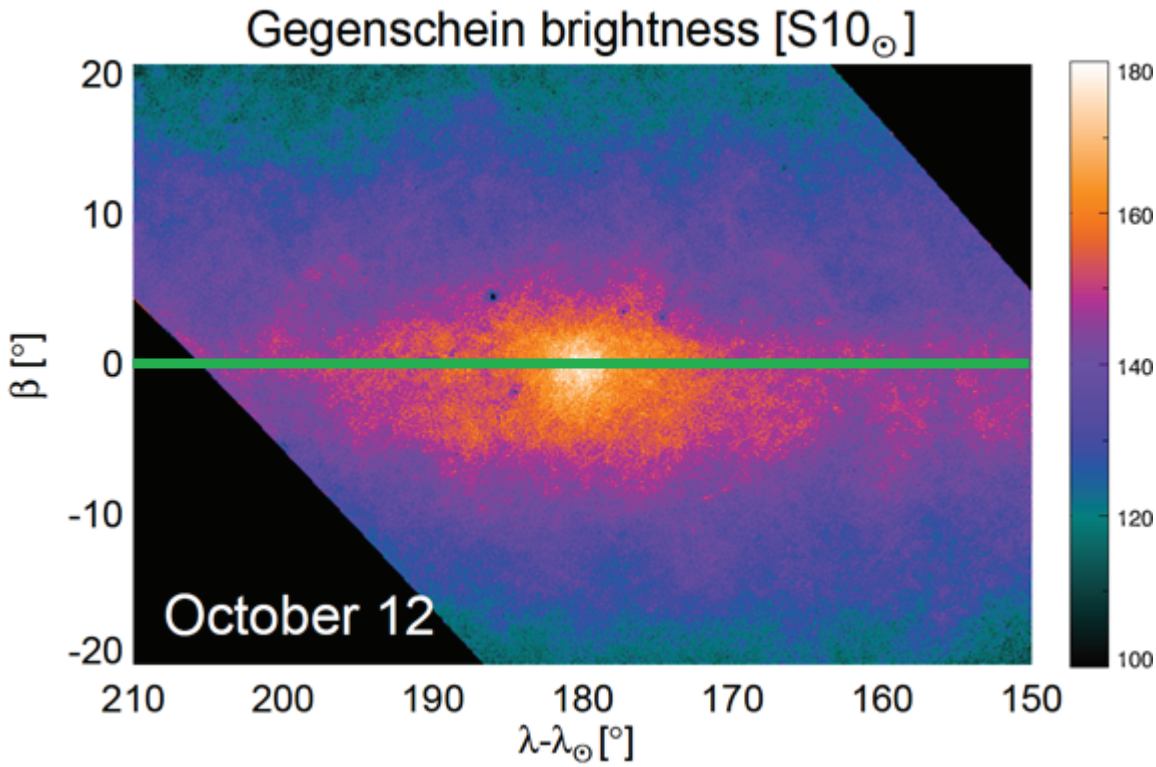

Figure 2.2. A color map of the Gegenschein. $\lambda - \lambda_\odot$ is the heliocentric ecliptic longitude, and β is the ecliptic latitude. The green line is the ecliptic plane.

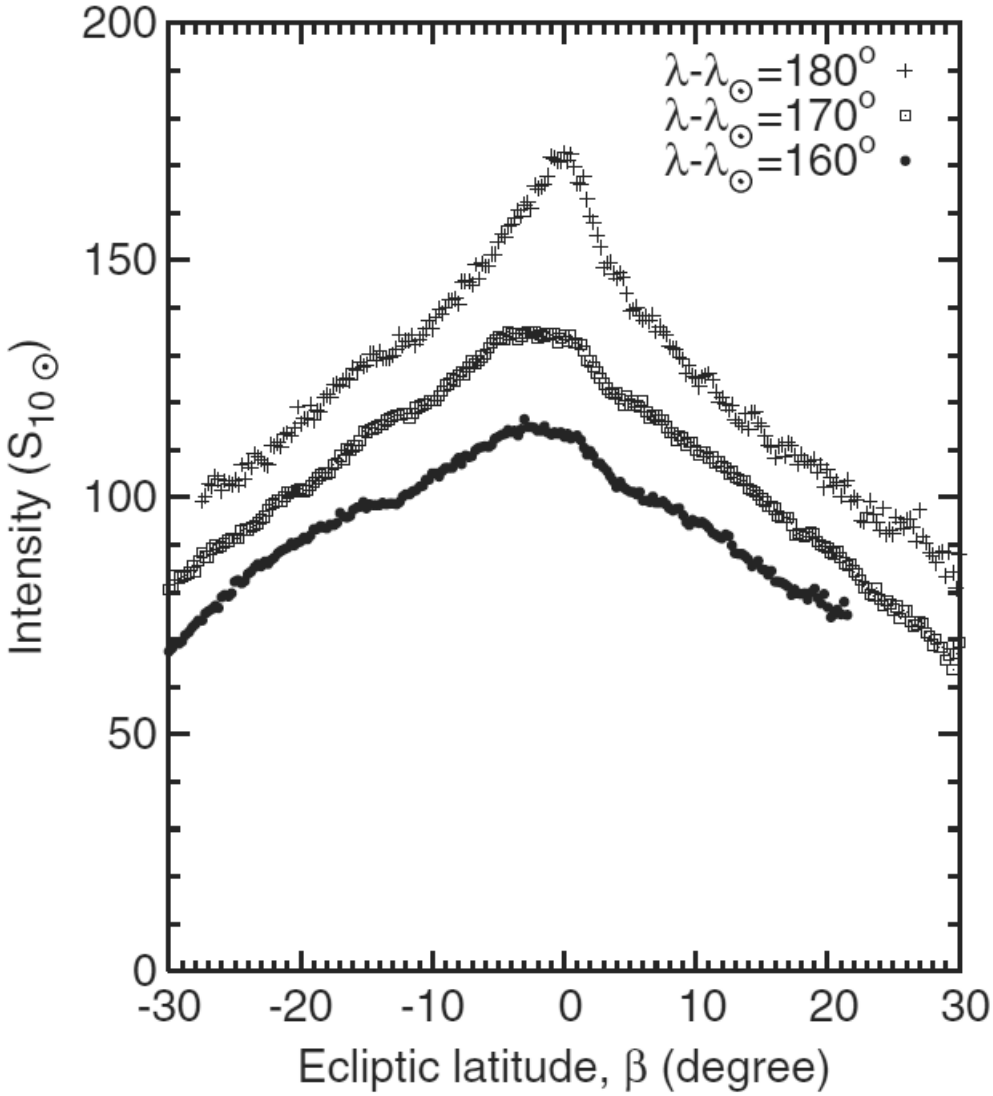

Figure 2.3. Surface brightness profile along the ecliptic latitude direction. Three lines indicate data in the ecliptic longitudes, $\lambda - \lambda_\odot$ is 180° (top), 170° (middle), 160° (bottom). The middle and bottom profiles are shifted downward for clarity, by 10 $S_{10\odot}$ (middle), and 20 $S_{10\odot}$ (bottom), respectively. (from Ishiguro et al. 2013)

light has primarily been measured at infrared wavelengths from space (Matsuura et al. 1995; Matsumoto et al. 1996; Fixsen & Mather 2002; Reach et al. 2003; Ootsubo et al. 2009; Tsumura et al. 2010). Since there is no spectroscopic data available in the optical wavelength range (as of 2015 November), we derived the optical spectral gradient S' by a log-linear fitting using compiled photometric data taken at different wavelengths around 4600 Å (Leinert et al. 1998). The regression formula for the ratio between the solar spectrum and the zodiacal light spectrum is given by

$$I_\lambda \propto \left[1.0 + 0.9 \times \log\left(\frac{\lambda}{5000\ \text{Å}}\right)\right] I_\odot \tag{2.2}$$

where I_λ and $I_\odot$ denote the flux densities of zodiacal light and the Sun at wavelength λ, respectively. Eq. (2.2) is applicable for zodiacal light in the spectral range of $\lambda \leq 5000$Å at a solar elongation of $> 90°$ (Leinert et al. 1998). From Eq. (2.2), we obtained the spectral gradient of IDPs as S'=$8.5 \pm 1.0\ \% \cdot 1000\ \text{Å}^{-1}$ at 4600Å. Note that we derived S' at 4600Å in order to match the measured wavelength of the albedo.

2.2.2 Albedo and spectral gradient for minor bodies in the solar system

Turning now to the IDP sources, we assume that they originate from asteroids and comets. In addition, some IDPs may originate from interstellar space (Hahn et al. 2002). For asteroids, we considered five major taxonomic types, namely, C-, X-, S-, B-, and D-types (DeMeo & Carry 2013), as input data. Since the optical properties of cometary nuclei are similar to those of D-type asteroids (one taxonomic type of asteroids), we do not discriminate between D-type asteroids and cometary nuclei. We thus assumed that IDPs consist of dust particles from six populations: C-type, X-type, S-type, and B-type asteroids, as representatives of asteroids, cometary nuclei (including D-type asteroids), and interstellar dust.

To create a template of the optical properties of the six potential dust sources, we made use of catalogs of albedos and the spectra of asteroids and comets. For asteroids, we used the Asteroid Catalog Using AKARI(AcuA) as a data set of albedos (Usui et al. 2011), and the SMASSII catalog as data sets of spectral gradients (Bus 1999; Bus & Binzel 2002a; Binzel et al. 2004). We found 274 C-type, 222 S-type, 191 X-type, 40 B-type, and 33 D-type asteroids archived in both catalogs. For C-type, B-type, and D-type asteroids, which show no obvious absorption, we used the spectral gradient values measured between 4350 and 9250Å (Bus & Binzel 2002a; Binzel et al. 2004). For the S-type and X-type asteroids, which may have an absorption band around > 7000 Å, we used the data at $4400 - 7000 Å$ (Bus 1999). Albedos and spectral gradients of 10 cometary

nuclei were compiled from various previous studies, shown in Table 2.1. For interstellar dust, we used the optical properties of average galactic dust particles at 4600 Å, that is, A=0.67 and S'=-23 ± 1 % $\cdot$ 1000 Å^{-1} (Draine 2003). We ignored some taxonomic types of asteroids, such as K-type, L-type, and V–type as discussed in Section 2.4.

Figure 2.4 shows the relationship between the albedos and spectral gradients for the IDPs and the potential parent bodies described above. In the diagram, the datum of IDPs is located within the population of comets and its spectral analog, D-type asteroids, suggesting that the major constituents are of cometary origin. In the following section, we will further investigate the contribution of each population using statistical analysis.

Table 2.1. Optical properties of cometary nuclei.

Name	Type	Albedo	Spectral Gradient	References
1P/Halley	Halley type	0.043	7.5	(a), (c), (g)
2P/Encke	Encke type	0.050	11	(h), (j), (r)
9P/Tempel 1	Jupiter family	0.056	12.5	(q)
10P/Tempel 2	Jupiter family	0.022	20	(e), (f)
28P/Neujmin 1	Jupiter family	0.025	11.8	(b), (k), (p)
49P/Arend-Rigaux	Jupiter family	0.028	10.4	(d), (i)
67P/Churyumov-Gerasimenko	Jupiter family	0.047	10	(o), (s), (t), (u)
103P/Hartley 2	Jupiter family	0.045	8.1	(v)
162P/Siding Spring	Jupiter family	0.034	9.2	(m), (n)
C/2001 OG_{108} (LONEOS)	Halley type	0.040	9	(l)

Note. — (a) Sagdeev et al. (1986), (b) Campins et al. (1987), (c) Keller et al. (1987), (d) Millis et al. (1988), (e) A'Hearn et al. (1989), (f) Jewitt & Luu (1989), (g) Thomas & Keller (1989), (h) Luu & Jewitt (1990), (i) Luu (1993), (j) Fernández et al. (2000), (k) Campins & Fernández (2002), (l) Abell et al. (2005), (m) Campins et al. (2006), (n) Fernández et al. (2006), (o) Lamy et al. (2006), (p) Campins et al. (2007), (q) Li et al. (2007), (r) Boehnhardt et al. (2008), (s) Lamy et al. (2008), (t) Tubiana et al. (2008), (u) Kelley et al. (2009), (v) Li et al. (2013)

2.2.3 Bayesian analysis

In this chapter, we limited the origins of IDPs cloud complex to six kind of source populations (C-, X-, S-, B-, D-types asteroids (including cometary nuclei), and interstellar dust particles) and investigated the probable fractional contributions of each populations. According to Bayes' theorem, the probability of a specific combination of fractional contributions is proportional to the probability of the specific combination generates observed optical properties of IDPs cloud complex. In this work, we calculated the latter probability through Monte Carlo (MC) calculation. If the MC calculations have done for multiple cases of specific fractional contributions, we can compare the probability of the fractional contributions through Bayes' theorem. We performed MC simulations for every possible combination of fractional contributions in a 2% interval.

When we chose objects from a type of population and calculated the correlation coefficients between the albedos and spectral gradients, the absolute values were as low as -0.14, -0.04, 0.16, -0.36, and -0.11, for the C-type, S-type, X-type, B-type, and D–type asteroids, respectively. Therefore, we considered these two properties, the albedo and spectral gradients, as independent of each other, and treated a probability of observed values as a product of probabilities of albedo and spectral gradient. Within a population, we simply assumed that the albedo follows a log-normal distribution, whereas the spectral gradient has a Gaussian distribution. We fit the distributions shown in Figure 2.4 to the model distributions shown in Figures 2.5 and 2.6. Because interstellar dust particles, which make only a limited contribution to IDPs, have optical properties that are very different from those of solar system objects, we assumed that the interstellar dust particles have a fixed albedo value of $A = 0.673$ and a spectral gradient of $S' = -23.2 \pm 0.8\ \% \cdot 1000\ \text{Å}^{-1}$ (Draine 2003), and we did not consider their statistical distributions in the following analysis. The optical properties of interstellar dust were estimated for average Milky Way dust, therefore interstellar dust in the solar vicinity may differ with the value. However, we ignored such possibility in this work.

We made a 2% grid for the possible combinations of fractional contributions from the source populations. Then, through linear combination of the probability distributions of the source populations according to the given contribution, we were able to generate a mixture probability distribution for an optical property of a single dust particle. Different populations were weighted according to their average albedos. From the probability distribution for a single particle, we calculated the expected average values of both the albedo and spectral gradient for the IDP complex using MC simulations. At every grid point, the average optical property value of 500 sample particles were calculated 3000 times. Under these conditions, the 3000 average values follow a Gaussian distribution

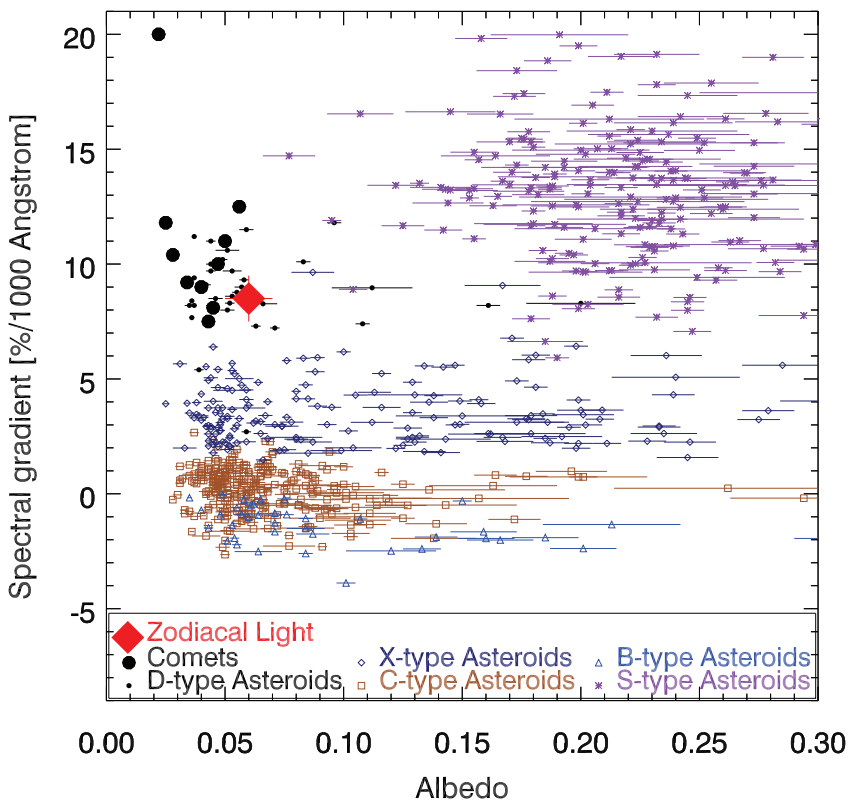

Figure 2.4. Spectral gradients S' with respect to the albedos A of asteroids, comets, and zodiacal light. Uncertainties of albedos are appended in the plot. The 1σ measurement uncertainties in spectral gradients are ordinarily about $0.7\ \% \cdot 1000\ \text{Å}^{-1}$.

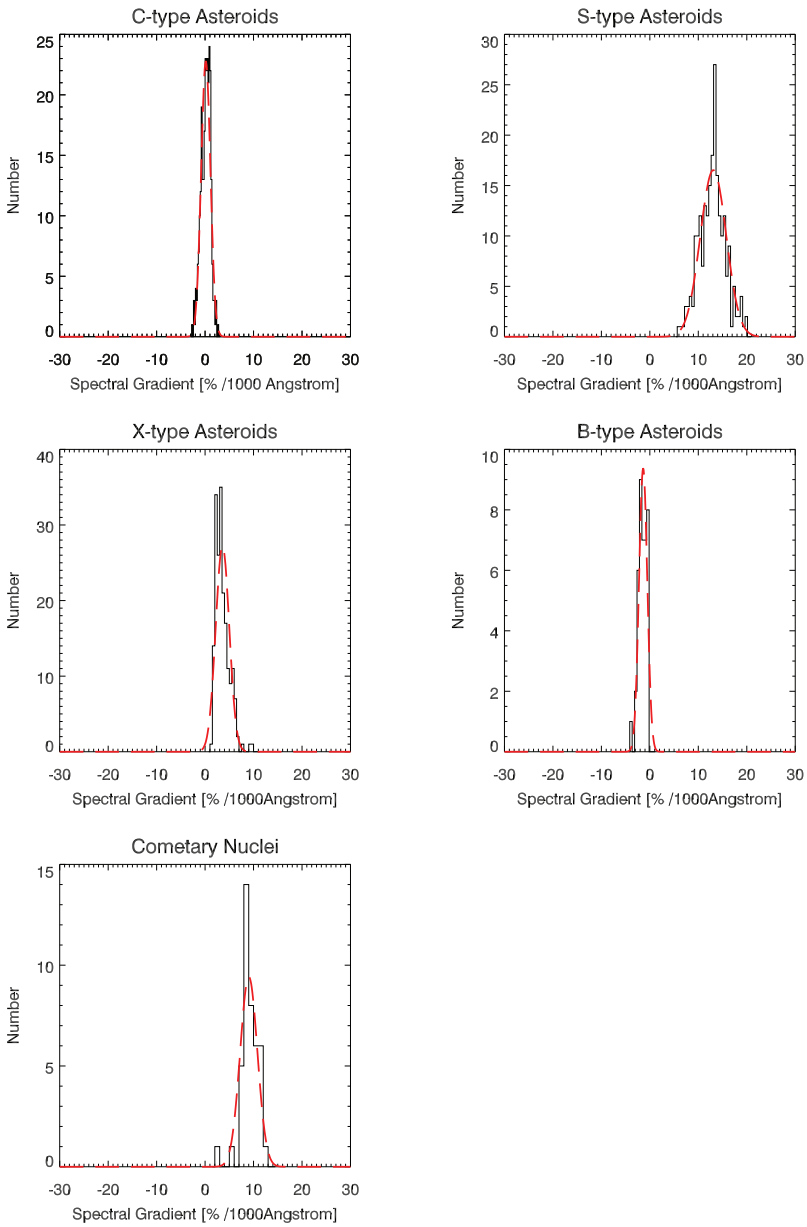

Figure 2.5. Albedo distribution of C-type, S-type, X-type, B-type asteroids, and cometary nuclei including D-type asteroids (Usui et al. 2011). Black solid lines are histograms for the given types. Red dashed lines are the log-normal distributions calculated from the mean and standard deviation of logarithms.

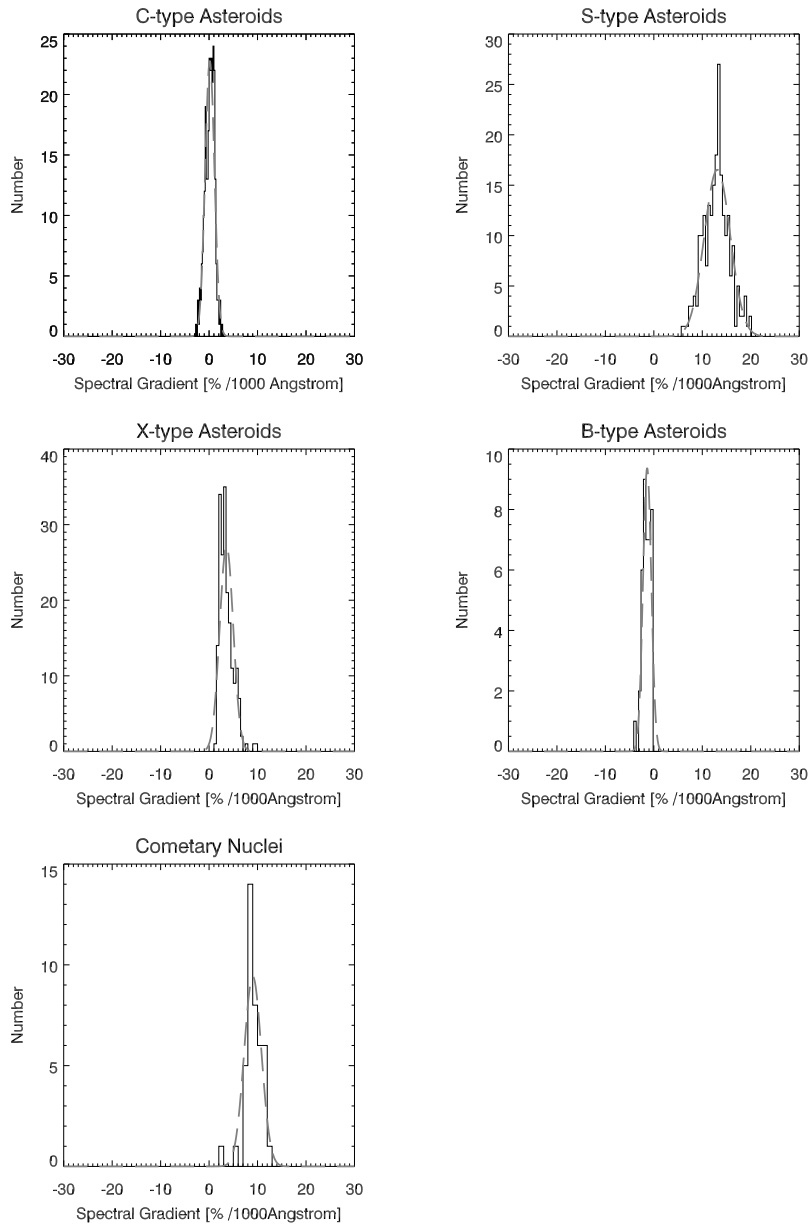

Figure 2.6. Spectral gradient distribution of C-type, S-type, X-type, B-type asteroids, and cometary nuclei including D-type asteroids (Bus 1999; Bus & Binzel 2002a). Black solid lines are histograms for the given types. Red dashed lines are the Gaussian distributions calculated from the mean and standard deviation.

Table 2.2. Contributions of Six Source Populations to the IDPs

Population	Contribution
Cometary nuclei	94^{+6}_{-26}%
B-type asteroids	4^{+18}_{-4}%
X-type asteroids	2^{+24}_{-2}%
C-type asteroids	0^{+26}_{-0}%
S-type asteroids	0^{+10}_{-0}%
Interstellar dust	0^{+2}_{-0}%

with a standard deviation of less than 10% of the uncertainty on the zodiacal light measurement. At each grid point, we compared the average value distributions in the MC simulations with the measured values of the zodiacal light with errors, and therefore derived probability that an observation of hypothetical IDPs cloud from the grid point resulted in the measured values. The probability was regarded as the probability of the grid point representing the real fractional contributions through a Bayesian analysis with a flat prior.

2.3 Results

Table 2.2 shows the resulting contributions from the individual sources to the IDP cloud. To derive the ranges (which are shown as plus and minus signs in the Table 2.2), we created contours with the same probability in the six-dimensional grid, calculated the total probability within the contours around the most probable case, and derived a range with a 68.3 % confidence interval. We found that cometary nuclei (including D-type asteroids) are the primary contributors ($\sim 94\%$) to the IDPs cloud as predicted in the Section 2.2. The remaining part ($\sim 6\%$) originates from the C-type, X-type, and B-type asteroids. S-type asteroids and interstellar dust make an insignificant contribution to the IDPs ($\sim 0\%$). Figure 2.7 shows the marginalized probability distributions of the four major populations.

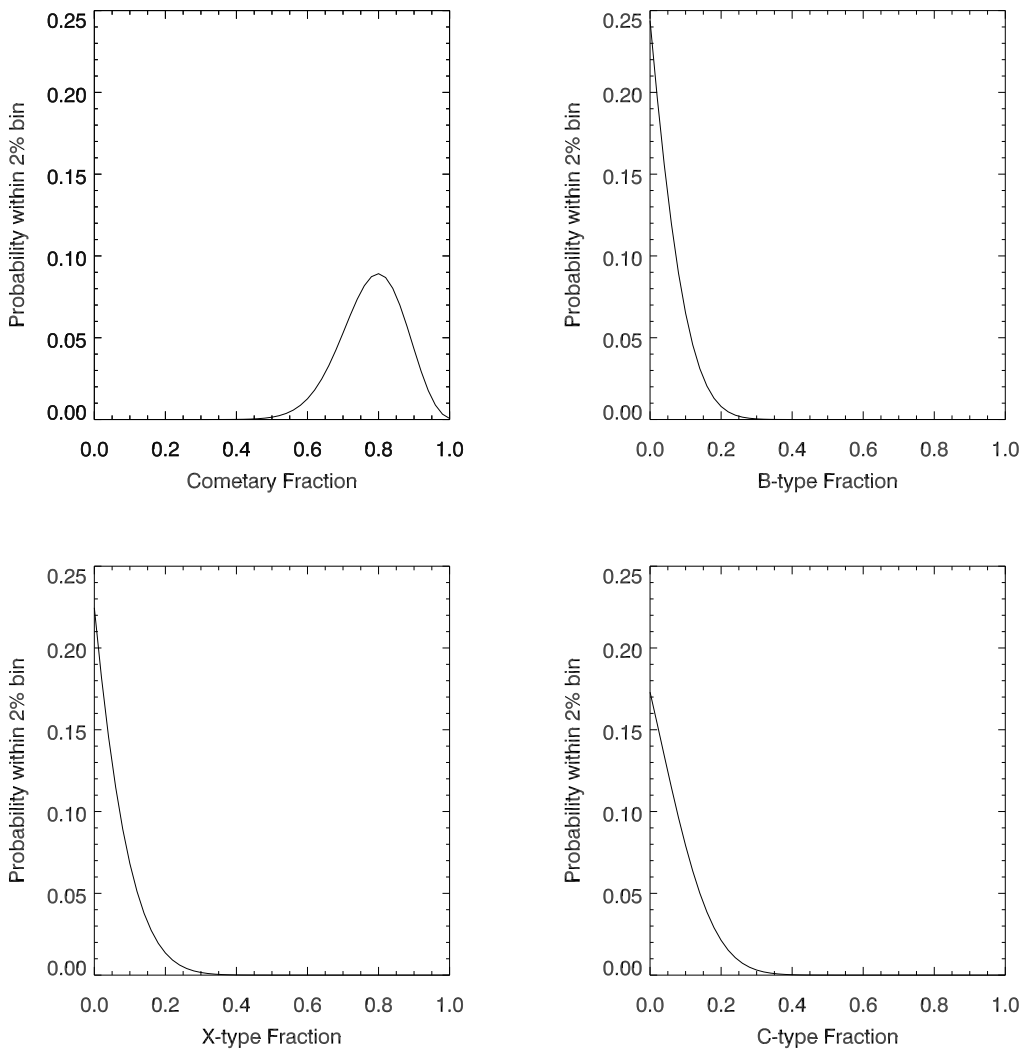

Figure 2.7. (a) - (d) Marginalized probability for the fractions of cometary (D-type asteroids), B-type, X-type, and C-type asteroids. The probability of the vertical axis is the values integrated over a 2% bin.

2.4 Discussion

2.4.1 Feasibility of the method

To assess the feasibility of our approaches described above, let us discuss the three following points.

First, we should consider the validity of the source populations. There is a wide variety of objects in the solar system, however, only six types of sources (five types of asteroids, comets, and interstellar dust particles) are considered in this dissertation. Recently, the mass fractions from different taxonomic types of asteroids were studied using new multifilter photometric survey data. DeMeo & Carry (2013) suggested that C-type asteroids account for more than 50% of the mass in the main belt. Although S-types, P-types, B-types, and V-types have moderate fractions ($\sim$10% each of the total mass of asteroids in the main belt), other asteroids, such as K-types, L-types, and A-types, only have minor contributions of $< 1\%$. P-types are included in X-types in our assumption. Thus, we considered all but one, namely, V-types, of the major asteroids in this paper. We conjecture that V-types cannot contribute to the IDP cloud because they have very large albedos ($A = 0.30$, Usui et al. (2011)). In addition, the mass fraction of V-types is very small (0.01%) when we exclude the largest objects in the taxonomic type (i.e., (4) Vesta). Meanwhile, the photopolarimeters on board the Pioneer 10 and 11 spacecraft revealed that the zodiacal light brightness is negligible beyond 3.3 AU (Toller 1981). Those observations suggest that the contribution from outer objects such as Kuiper-belt objects (KBOs) may not be as large as those from asteroids when we consider the previous dynamic studies pointing out that the dust particles from KBOs have peak densities outside of the Jovian orbits (Poppe & Horányi 2012; Vitense et al. 2014). The optical properties of the Centaurs show bimodality. Inactive Centaurs show ultra-red spectra similar to KBOs, and active Centaurs have colors and albedos similar to cometary nuclei (Stansberry et al. 2008; Melita & Licandro 2012). In this paper, inactive ultra-red Centaurs were ignored along with KBOs, and active Centaurs were treated as cometary nuclei. Some cometary nuclei have optical properties that are different from those of D-type asteroids, as in the cases of 95P/Chiron and 107P/Wilson-Harrington. We did not include these kinds of objects in this study. We do not know how many of such objects exist, but these non D-type asteroidal nuclei are similar to other kinds of asteroidal groups in terms of their optical properties. Therefore, each population of an asteroidal group should be understood to include possible cometary nuclei whose optical properties are similar to the group. If we subdivide the X-type asteroids into E-type, M-type, and P-type asteroids, the results remains same, with only the confidence

interval worsening because the optical properties of P-type asteroids are similar to those of D-type asteroids.

Second, we should consider the time-evolution of the optical properties via space weathering. We assumed that the optical properties of dust particles resemble those of the source objects. However, this may not be true in some populations. Since the Poynting–Robertson lifetime of silicaceous dust particles 1 mm in size is about 2×10^7 years when released into a circular orbit from 2.5 AU (Mann et al. 2006), while the timescale of space weathering is more than an order of magnitude shorter than this lifetime (Shestopalov et al. 2013, $\sim 7 \times 10^5$ years for S-type asteroids), it is reasonable to assume that surfaces on both silicaceous IDPs and S-type asteroids are altered by space weathering and therefore have similar optical properties. However, the space weathering of C-type, X-type, and B-type asteroids is not well known, although there are studies, e.g. Moroz et al. (2004). Therefore, we cannot clearly discuss the optical surface maturation of IDPs originating from these asteroids. Furthermore, cometary dust particles remain within the interplanetary space longer than the active lifespan of cometary nuclei (Levison & Duncan 1997, ∼12,000 years for the ecliptic comets); therefore, the relation between the optical properties of cometary dust particles and the surfaces of active cometary nuclei is not direct. If we regard the cometary nuclei and D-type asteroids as identical, then there are studies that imply that the spectra of D-type asteroids would not change significantly over time. D-type asteroids were found in the inner main belt (DeMeo et al. 2014), and Phobos, possibly a captured D-type asteroid, has the optical properties of a D-type asteroid after remaining in the inner solar system for billions of years (Pajola et al. 2013, 2014). Even though these objects have albedo values slightly higher than the average for D-type asteroids, their albedos and spectral gradients are still in the range of D-type asteroids. In another direction, according to the laboratory experiments on the Targish Lake meteorites, which have spectra similar to D-type asteroids, the continuum spectrum moved in the bluer direction after being exposed to laser radiation (Hiroi & Sasaki 2012). If these results can be applied in our case, then the contribution of cometary nuclei would increase. If we think about the cometary contribution which is dominant even now, then we can conclude that this assumption does not alter the conclusion of this paper.

Third, we should consider the effects of simplification in this study. We assumed that optical properties are randomly dispersed within a population, however, this may not be true. As shown in Usui et al. (2013), there is a relation between orbital elements and optical properties. We want to emphasize that the differences in the optical properties between different types of sources are an order of magnitude larger than the differences

between the sub-groups of different types of sources, as shown in Figure 2.4. Furthermore, we ignored the weak correlation between the albedo and the spectral gradient. This relation was non-negligible for B-type asteroids. There is a possibility that the interstellar dust, which entered the solar system, has a different composition compared to the average dust particles in the Milky Way galaxy (Mann 2010), but we ignored this possibility. However, we justify these simplifications because the contributions from B-type asteroids and interstellar dust are almost negligible. The SMASSII catalog is not bias-free (Mothé-Diniz et al. 2003), and we do not know the optical properties of unbiased populations, but we ignored the effect of bias. We hope that the large measurement uncertainties in the optical properties of zodiacal light cover the consequences of the bias.

2.4.2 Comparison with IDP samples

Nowadays, IDPs are collected in the Antarctic ice or in the stratosphere around 20–25 km altitude using aircrafts, and they are well studied through laboratory investigations (Brownlee 1985; Engrand & Maurette 1998). Because such particles should contribute to the zodiacal light before they arrive on Earth, it is important to compare our result with IDP samples. It is known that there are two major IDP groups, referred to as "chondritic smooth" (CS) and "chondritic porous" (CP). CS IDPs are composed of low-porosity materials, predominantly hydrated layer silicates (Sandford & Walker 1985). CP IDPs have large porosities of about $\sim$70%. CP IDPs are dominated by anhydrous minerals. It is likely that CP IDPs originate from comets based on their mineralogical and petrographical properties (Bradley 2003). When the Earth passed through the dust stream of 26P/Grigg-Skjellerup (one of the JFCs), it was expected that 1%–50% of the total collected dust larger than 40 μm could originate from that comet (Messenger 2002). These were actually CP type IDPs of primitive anhydrous composition, supporting the assumption that CP IDPs are of cometary origin (Busemann et al. 2009). CS IDPs are thought to be derived from primitive (not differentiated) asteroids because comets do not exhibit the spectral signatures of hydrated silicate while asteroids do (McAdam et al. 2015).

Bradley et al. (1996) measured the reflectance spectra of IDP samples in the optical wavelength and found that CS IDPs generally exhibit flat spectra with a weak fall-off from 6000Å toward 8000Å (similar to CI and CM meteorites or C-type asteroids with $S' \sim 0$), whereas CP IDPs exhibit upward spectra ($S' > 0$) without remarkable curvature, although these IDP samples have a variety of albedo values and spectral slopes. Figure 2.8 compares the synthesized spectrum of zodiacal light based on our mixture model of small bodies with those of most typical CS IDPs (W7040A15) and

CP IDPs (W030A5) (Bradley et al. 1996). In Figure 2.8, we also show the input spectrum obtained from multi-band photometry in Leinert et al. (1998) and anti-solar point observation (Ishiguro et al. 2013). The synthesized spectrum of zodiacal light is similar to that of CP IDPs (W030A5) in that it shows a low albedo value and positive slope ($S' > 0$), but it is different from that of CS IDPs in that it does not show a positive slope beyond $\sim 6500\mathring{A}$. It should be noted that the fall-offs below 4500Å in IDP signals are artifacts of the measurements caused by small size effects and should be ignored in the comparison (Bradley et al. 1996). The spectral similarity leads to our assumption that the interplanetary dust complex is dominated by CP IDPs (i.e., the dominance of cometary particles in the zodiacal cloud). It is also curious that CP IDPs tend to have cluster structures of 20-100 μm (Bradley et al. 1996). The size is in agreement with the effective size of zodiacal light dust particles evaluated by the IDP size distribution model (Grün et al. 1985).

There seems to be a difference in the quantitative estimates of IDP origins between laboratory investigations of IDP samples and ours. Bradley (2003) studied 200 chondritic IDPs from the stratosphere and found that about a half of them are classified as CP IDPs. Similarly, Noguchi et al. (2015) investigated micrometeorite samples in Antarctica and suggested that $\sim 25\%$ or even less are categorized into CP IDPs. While we acknowledge that these laboratory investigations provide reliable results regarding the fraction of CS and CP IDPs fallen to Earth, we would draw attention to the sampling bias of the laboratory studies of IDPs. Asteroidal dust particles could be collected on Earth more selectively than cometary dust particles because of the orbital properties. The impact cross-section of asteroidal dust particles at Earth is a few times larger than that of cometary ones. Furthermore, the impact cross-section of Earth can be a few thousand times larger for dust particles trapped in quasi-satellite resonance, which favors asteroidal particles (Kortenkamp 2013).

2.4.3 Comparison with previous studies

Our results are in agreement with kinematic, dynamical studies based on the spatial distribution of zodiacal light (Nesvorný et al. 2010). The numerical simulations of Nesvorný et al. (2010) concluded that $\gtrsim 90\%$ of the zodiacal emission comes from IDPs originating from JFC, and $\lesssim 10\%$ from the Oort cloud comets or asteroids. These results agree with our result of a $> 90\%$ cometary contribution. However, we could not optically distinguish between different sub-populations of comets in this study. Therefore, we cannot know how large of a fraction of cometary IDPs originated from JFCs.

We compared our results with infrared spectroscopic observations of zodiacal light.

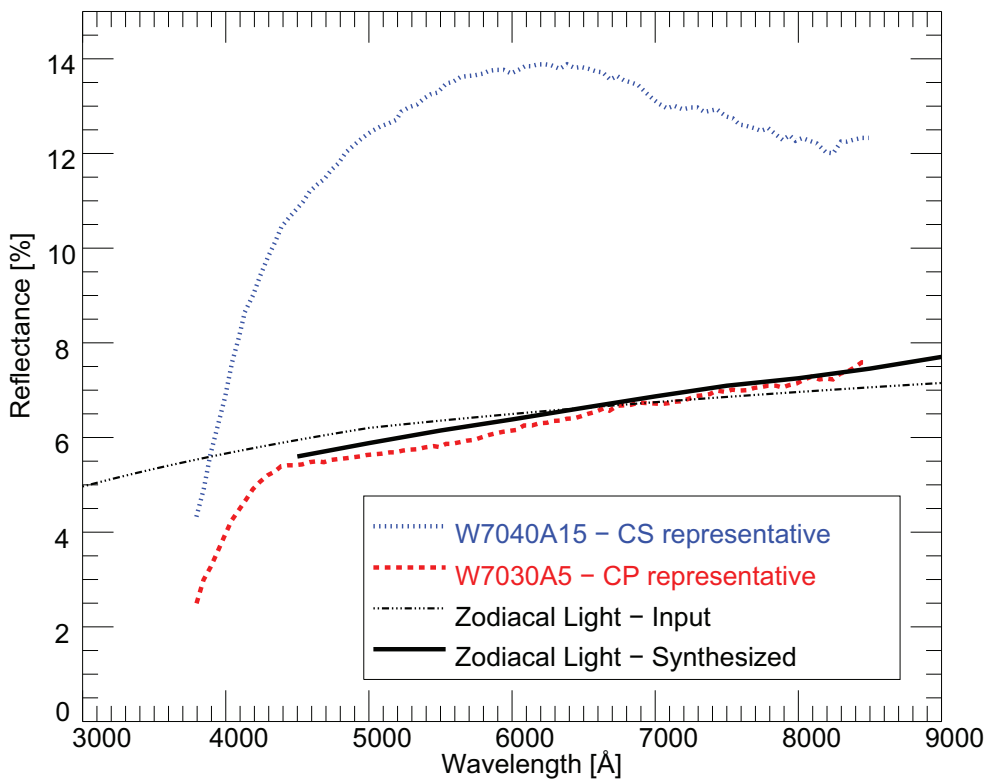

Figure 2.8. Comparisons of spectra between our synthesized zodiacal light model (thick continuous line) and CS and CP IDPs (dotted and dashed lines; Bradley et al. (1996)). The observed reference spectrum of zodiacal light is also shown (see Section 2.2.1). Note the drop-offs in the IDP spectra for less than 4000 Å artifacts.

By using mean albedo values and contributions from this study and adopting a typical visual-infrared spectrum of the populations from Bus & Binzel (2002b), we synthesized the model spectrum of zodiacal light and extrapolated it to the near-infrared wavelength, as shown in Figure 2.9. At wavelengths shorter than 1.6 μm, the overall observed NIR spectra of the zodiacal light (Tsumura et al. 2010) are similar to that of the synthesized spectra, but have absorption-like dark wavelengths around 1.3–1.4 μm. In this wavelength regime, the spectra of average B-type, C-type, and X-type asteroids are bluer than those of zodiacal light, as expected in this study. The observed spectra have large uncertainties at wavelengths longer than 1.6 μm. It is therefore difficult to form a clear conclusion, but the observed spectra are closer to those of D-type, C-type, or X-type asteroids than to those of S-type or B-type asteroids. Overall, the synthesized spectrum in this work is consistent with the observed spectrum from rocket-borne observations (Matsuura et al. 1995; Tsumura et al. 2010) and recent space observations of AKARI (Tsumura et al. 2013), but it does not agree with the space observation of IRTS (Matsumoto et al. 1996). The observed NIR spectra of zodiacal light are similar to those of D-type asteroids or cometary nuclei, which is in agreement with this work. Keeping in mind that we applied extrapolation through the model from optical observation, this match in the NIR reflected spectrum supports our conclusion of a dominant cometary contribution.

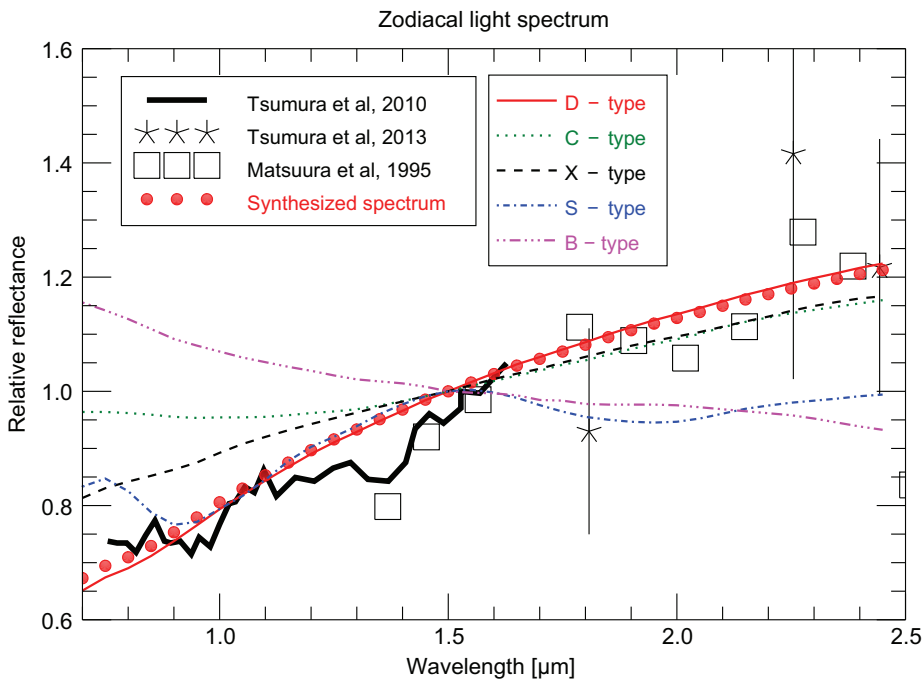

Figure 2.9. Comparison of near-infrared zodiacal light spectra between our synthesized model and observed data (Matsuura et al. 1995; Tsumura et al. 2010, 2013). The S-220-11 rocket data at an ecliptic latitude of 10° from Matsuura et al. (1995) were used in the figure. The template spectra of each type of asteroid are from Bus & Binzel (2002b), and the solar spectra are from Gueymard (2004). The templates, synthesized spectra, and the data from Tsumura et al. (2010) are normalized at 1.5 μm, and the data from Matsuura et al. (1995) and Tsumura et al. (2013) are scaled to match our model spectrum at 1.8–2.5 μm.

Chapter 3

Evolution of cometary dust particles to the orbit of the Earth: particle size, shape, and mutual collisions

[1]

3.1 Introduction to chapter 3

During the first half of 20th century, it became evident that dust particles ejected from solar system objects that are not the Sun itself are scattered in interplanetary space and are therefore observed as zodiacal light (by reflecting sunlight) and meteors (through encounters with the Earth) (Fechtig et al. 2001, and references therein). At the same time, it was found out that because of the Poynting-Robertson (P–R) effect and solar wind drag, those particles are falling to the Sun on a timescale shorter than $\sim 10^7$ years, which is ≈2–3 orders of magnitude shorter than the age of the solar system (Mann et al. 2006). Therefore, recent or continuous dust sources are required to explain the existence of the IDPs cloud complex at the current epoch. For the source of the IDPs, Nesvorný et al. (2010) argued that approximately 90 % of the IDPs are originated from comets by connecting the vertical brightness profiles of observed mid-infrared zodiacal light with those of their numerical models. We came to a similar conclusion in the previous chapter

[1] This chapter was written based on a manuscript accepted for publication in Astrophysical Journal on January 25, 2018. (Yang & Ishiguro 2018)

(i.e., > 90 % from comets) through a comparison between the observed optical properties (i.e., albedo and optical spectral gradient) of zodiacal light and those of different kinds of minor solar system bodies (Yang & Ishiguro 2015). In contrast, there are studies that have suggested a non-negligible fraction of asteroidal particles in the IDP cloud. Ipatov et al. (2008) examined the Doppler shifts of zodiacal light's Mg I Fraunhofer line and contrived an IDP cloud model that consisted of $30-50\%$ of asteroidal particles. Kawara et al. (2017) analyzed the UV–optical spectrum of zodiacal light taken with the Hubble Space Telescope and insisted that the spectrum is similar to that of C-type asteroids.

Under these circumstances, Nesvorný et al. (2011) reproduced observed helion meteor orbital distribution from dust ejected from Jupiter Family Comets (JFCs). However, as Ueda et al. (2017) indicated, recent in situ measurements by *Rosetta* at the coma of 67P/Churyumov-Gerasimenkoby (Rotundi et al. 2015; Fulle et al. 2015; Hilchenbach et al. 2016; Fulle et al. 2016a; Bentley et al. 2016; Agarwal et al. 2016; Mannel et al. 2016; Merouane et al. 2016) suggested that initial dust density and SFD are different from those in Nesvorný et al. (2011)'s initial condition. Furthermore, the in situ measurements by *Giotto* mission (Fulle et al. 1995) and *Stardust* mission (Green et al. 2004, 2007) as well as the IR observation (Vaubaillon & Reach 2010) unanimously determined SFD similar to that determined by *Rosetta* mission, even though the authors studied different comets (1P/Halley, 81P/Wild 2, and 73P/Schwassmann-Wachmann 3). Therefore, a careful treatment or explanation of these initial conditions is required to further confirm the cometary origin of IDPs. In this work, we investigated this question by introducing fluffy aggregates discovered in the Earth's stratosphere (Bradley 2003) and the coma of 67P/Churyumov-Gerasimenko (Fulle et al. 2015; Bentley et al. 2016; Mannel et al. 2016).

Total mass budget of the IDP cloud complex is also an important factor in characterizing the various physical processes because it is determined by a balance of every dust supply and removal processes in the solar system. Nesvorný et al. (2011) estimated the total mass ejection rate to the IDP cloud complex as $10^3 - 10^4$ kg s^{-1}. In this work, we revisited this budget with modified initial conditions.

Regarding the sink, it has been thought that catastrophic mutual collisions would be a dominant mechanism breaking IDPs of the size range of > 200 μm (Dohnanyi 1978; Grün et al. 1985; Steel & Elford 1986). Whereas these studies were targeted for IDPs on fixed circular orbits, their results were considered in previous dynamical research about IDPs on eccentric cometary orbits (Wiegert et al. 2009; Nesvorný et al. 2011; Pokorný et al. 2014). However, even though these authors did not pursue the reason, recent studies have reported that their results can be explained better when the actual collisional lifetime is

longer than that in Grün et al. (1985) (Nesvorný et al. 2011; Jenniskens et al. 2016, for example). Under this circumstance, Soja et al. (2016) calculated collisional lifetime of IDPs on fixed eccentric orbits, and reported collisional lifetime longer than Grün et al. (1985). Therefore, it is time to investigate the probability of mutual collisions under more realistic situations, IDPs on orbits which are initially eccentric and evolving under planetary perturbation and radiational acceleration.

In this study, we numerically examined the evolution of dust particles ejected from cometary nuclei. Through this work, we tested a wide variety of initial conditions, namely orbits, dust shape, density and the SFD. We investigated different evolutionary tracks according to initial orbits and dust particle cross-section to mass ratios. Then, we searched for valid combinations of dust particles with different particle shape, density and initial SFD values, considering the in situ measurements by the spacecrafts. The required mass budgets of the IDP cloud complex were derived for valid cases. Finally, we estimated the probability of mutual collisions among dust particles. Note that this is the first attempt to connect the dust SFD of cometary comae with the SFD around the Earth. This work is also the first attempt to derive the probability of mutual collisions in a direct manner via numerical simulation. The description of our methodology is presented in section 3.2. In subsection 3.3.1, We examine different evolutionary tracks under different initial conditions: particles ejected from JFCs or 2P/Encke–like objects; particles with small or large radiative acceleration to gravitational acceleration ratios. In subsection 3.3.2, we show the possible combinations of evolutionary tracks under different initial conditions, including particles that are compact or fluffy, particles with high or low particle densities, and different forms of initial SFD. We show the expected mass supply rate for the possible combinations in subsection 3.3.3. We estimate the probability of mutual collisions among IDPs with respect to the source orbits, particle sizes, and particle shape in subsection 3.3.4. In section 3.4, we considered relative contribution from different initial orbits, particle size, and particle shape to the zodiacal light brightness and density near the Earth's orbit along with the total mass supply rate.

3.2 Methodology for the dynamical model

3.2.1 Numerical Integration

In our model, we ejected hypothetical dust particles from the orbits of selected 'actual' comets. We considered nine different β values, ratios of the solar radiative acceleration with respect to the solar gravitational acceleration: $\beta = 0.57$, 0.285, 0.114, 0.057, 0.0114,

0.0057, 0.00285, 0.00114, and 0.00057. β is defined as

$$\begin{aligned}\beta &\equiv \frac{F_{rad}}{F_{grav}} \\ &= (3L/16\phi GMc)(Q_{pr}/\rho s) \\ &= 5.7 \times 10^{-5} Q_{pr}/\rho s,\end{aligned} \tag{3.1}$$

where L, M, G, c, ρ, and s denote solar luminosity, solar mass, gravitational constants, light speed, mass density, and spherical particle radius, respectively. The radiation pressure coefficient Q_{pr} is given by $Q_{pr} = Q_{abs} + Q_{sca}(1 - < cos\ \alpha >)$, where Q_{abs}, Q_{sca}, and α denote absorption coefficient, scattering coefficient, and scattering angle, respectively (Burns et al. 1979). When spherical particles with a density of 0.8 g cm^{-3} is assumed, as we can obtain from equation 3.1, that these β values are equivalent to diameters of 2.5, 5, 12.5, 25, 125, 250, 500, 1250, and 2500 μm. The details about source selection and dust ejection will be explained in the next subsections. All dust particles were ejected at the same epoch, a Julian date of 2457054.5 (A.D. 2015, February 1, 0:00) for convenience in our simulation. Planetary ephemerides for each epoch were calculated by an N-body simulation using the initial data in Chambers (1999). During the numerical calculation of the orbital evolution of dust particles, we accounted for the Sun and eight planets as massive objects that exert gravitational accelerations and ignored the gravitational effects of other objects. In addition, radiative acceleration, including P–R drag due to solar radiation, was considered, while these effects due to other sources were ignored because of their weakness. Solar radiation was treated as constant over time. The effect of solar wind drag is assumed to be proportional to 30 % (Gustafson 1994) of the P–R drag (Burns et al. 1979). Consequently, the equation of motion for particles can be written as the following form:

$$\ddot{\boldsymbol{r}} = -\frac{GM}{r^2}\left[(1-\beta)\boldsymbol{e_r} - (1+f)\beta\left(\frac{\dot{r}}{c}\boldsymbol{e_r} + \frac{\boldsymbol{v}}{c}\right)\right] + \sum_{i=1}^{8}\frac{GM_i}{{r_i}^2}\boldsymbol{e_{r_i}}, \tag{3.2}$$

where, $\boldsymbol{r}$ represents position vector of the dust particle, and $\boldsymbol{v}$ denotes velocity vector of the particle. The factor f is a ratio between solar wind drag and P–R drag. The first term in the square bracket describes a effective solar gravity reduced by the radiational pressure. The second term in the bracket describes the terms for P–R effect and solar wind drags. The final term represents the gravitational perturbations from 8 planets. Equation 3.2 was derived based on Burns et al. (1979). Recently, Klačka et al. (2014) derived another equation of motion which describes P–R drag more rigorously, however,

the difference between two equations of motion is negligible at the speed range of the solar system object (Burns et al. 2014). We employed a numerical integrator applying the RADAU15 algorithm (Everhart 1985), originally coded by Chambers (1999, MERCURY 6.2), and modified by Jeong (2014) for taking into account the radiation effects. Dust particles were excluded from the calculation when the heliocentric distance became larger than 80 au or smaller than 0.05 au. The initial integration time step was 3.6525 days, and the variable time step was chosen to accomplish an accuracy of at least $| \Delta E/E | \leq 10^{-12}$ in energy during a single step. We stopped integrations after 2 million years, when most dust particles were excluded from the numerical integration by the above conditions.

3.2.2 Source Population

According to previous research (Tancredi et al. 2006; Snodgrass et al. 2011), even though JFCs have not been completely surveyed, it is suggested that the distribution of known JFCs is less observationally–biased, and therefore, the SFDs of all known JFCs and those of JFCs with small perihelion distances are statistically same (Fernández et al. 2013), implying that known JFCs can statistically represent the whole population. Therefore, supposing that JFCs are the main source of the IDP cloud complex, we began our simulation from existing cometary nuclei. Furthermore, we assumed that number of comets has been constant over a few million years as we explain in subsection 3.2.4. This approach of source selection is basically similar to but slightly different from the idea in Wiegert et al. (2009). The difference in source selection between Wiegert et al. (2009) and this work lays in three parts. Firstly, they assumed that all asteroid population in their model eject a small amount of dust particles as a result of mutual collisions, whereas we regarded that active asteroids (instead of entire asteroid population) eject dust particles. Secondly, we considered small dust particles with large cross-section (i.e., β >0.057) which were not considered in Wiegert et al. (2009). Lastly, we included 3 times as many comets as Wiegert et al. (2009) did. We chose the source comets from the JPL Horizons comet list as of 2015 January 23 (http://ssd.jpl.nasa.gov/dat/ELEMENTS.COMET).

Among the 3,321 comets in the list, we chose periodic comets with eccentricity $e < 1$ and excluded fragments to avoid duplication from dust particles from the same comets. In total, we chose 1,049 comets for consideration. We classified these comets into JFCs, Encke Type Comets (ETCs), Chiron Type Comets (CTCs) and Halley Type Comets (HTCs) following the criteria in Levison (1996). HTCs were further classified into two classes: one with the semimajor axis a larger than that of Jupiter a_{J} (HTC-1) and another with $a \leq a_{\mathrm{J}}$ (HTC-2). ETCs were further categorized into two classes: one case having a Tisserand parameter with respect to Jupiter of $T_{\mathrm{J}} < 3.01$ (ETC-1), another

with $T_{\rm J} \geq 3.01$ (ETC-2). In our simulation, dust particles from ETC-1 experienced close encounters with Jupiter and had similar evolutionary tracks to dust particles from JFCs. Dust particles from ETC-2 are less influenced by close encounters with Jupiter. Note that this criteria is different from the working definition of active asteroids (AA), that is, $T_J \geq 3.08$ (Jewitt et al. 2015) because our concern is not the orbital similarity with asteroids but the dynamical interaction with the Jupiter. The orbit of 2P/Encke is largely different from AAs (occasionally referred to as main-belt comets) in that 2P/Encke has a large eccentricity and a short perihelion distance. However, dust particles from 2P/Encke are less susceptible to close encounter with the Jupiter, similar to AAs. For this reason, both 2P/Encke and AAs are categorized into the same group (ETC-2) in our definition.

In orbital elements space, we constructed 17 step bins for semimajor axis a (0.0–0.5, 0.5–1.0, 1.0–1.5, 1.5–2.0, 2.0–2.5, 2.5–3.0, 3.0–3.5, 3.5–4.0, 4.0–4.5, 4.5–5.0, 5.0–7.0, 7.0–9.0, 9.0–14.0, 14.0–19.0, 19.0–24.0, 24.0–30.0, 30.0–40.0 in au), 5 bins for eccentricity e (0.0–0.2, 0.2–0.4, 0.4–0.6, 0.6–0.8, 0.8–1.0), and 6 bins for inclination i (0.°0–30.°0, 30.°0–60.°0, 60.°0–90.°0, 90.°0–120.°0, 120.°0–150.°0, 150.°0–180.°0), and counted the number of cometary orbits within each bin three dimensionally. Under the choice of bins, each box includes 0 to 63 cometary orbits. In each box, we chose comet samples as representatives of whole population of the given orbital class and performed the numerical calculation with their orbital elements. To eliminate sampling bias and reduce computational load, we chose multiple samples in a box if the number of orbits in a box is larger than 5.5% of the total number of JFCs, ETC-1s, ETC-2s, and HTC-2s. In the assumption, we implied that dust ejected from other comets in the box should experience orbital evolution similar to those of representative comets. Table 3.1 shows the list of selected comets included in the calculation and their weighting factor w_i, which is the number of comets whose dust particles are assumed to have similar evolution with the particles from the listed comets. Later in subsection 3.2.4, when we made clones of cometary dust particles, the number of clones was determined to be proportional to w_i. The orbital elements of selected comets, 64 JFCs, 45 HTC-1s, 2 HTC-2s, 3 ETC-1s, 6 ETC-2s, and 6 CTCs are listed in Table 3.1 along with their w_i values.

As mentioned above, we assumed that our sample of JFCs, HTC-2s, ETC-1s, and ETC-2s is free from discovery bias and used the data in making the IDP cloud complex model in subsection 3.2.4. CTCs and HTC-1s were not included in the model but are referred to for comparison. The orbital distribution of these comets is shown in Figure 3.1. As a comparison (see Tables 3.2–3.3), we also performed a numerical simulation of asteroidal dust particles. We tested a simple situation in which one dust particle per β value was ejected from the largest 1933 asteroids (>15 km in diameter), considering that

these large asteroids are completely detected.

Table 3.1. List of comets included in our numerical simulation

Name	Orbital type[a]	q^b [au]	e^c	i^d [°]	w_i^e
3D/Biela	JFC	0.879	0.751	13.2	6
4P/Faye	JFC	1.66	0.569	9.05	21
5D/Brorsen	JFC	0.590	0.810	29.4	3
6P/d'Arrest	JFC	1.36	0.611	19.5	6
7P/Pons-Winnecke	JFC	1.24	0.638	22.3	11
9P/Tempel 1	JFC	1.53	0.512	10.5	16.67
10P/Tempel 2	JFC	1.42	0.537	12.0	16.67
14P/Wolf	JFC	2.74	0.356	27.9	28
15P/Finlay	JFC	0.976	0.720	6.80	11
16P/Brooks 2	JFC	1.47	0.563	4.25	16.67
17P/Holmes	JFC	2.06	0.432	19.1	21
18D/Perrine-Mrkos	JFC	1.27	0.643	17.8	6
19P/Borrelly	JFC	1.35	0.626	30.4	2
29P/Schwassmann-Wachmann 1	JFC	5.76	0.0419	9.38	5
30P/Reinmuth 1	JFC	1.88	0.501	8.12	21
31P/Schwassmann-Wachmann 2	JFC	3.42	0.194	4.54	5
32P/Comas Sola	JFC	2.00	0.556	9.97	4.67
33P/Daniel	JFC	2.17	0.462	22.4	15
34D/Gale	JFC	1.18	0.761	11.7	9
42P/Neujmin 3	JFC	2.01	0.585	3.99	4.67
53P/Van Biesbroeck	JFC	2.43	0.551	6.61	15
56P/Slaughter-Burnham	JFC	2.53	0.504	8.16	15
59P/Kearns-Kwee	JFC	2.36	0.475	9.34	15
63P/Wild 1	JFC	1.95	0.651	19.8	21.5
64P/Swift-Gehrels	JFC	1.38	0.690	8.95	9
65P/Gunn	JFC	2.87	0.261	9.24	14
72P/Denning-Fujikawa	JFC	0.784	0.819	9.17	1
76P/West-Kohoutek-Ikemura	JFC	1.60	0.539	30.5	2
79P/du Toit-Hartley	JFC	1.12	0.619	3.15	10

Table 3.1 (cont'd)

Name	Orbital type[a]	q^b [au]	e^c	i^d [°]	w_i^e
91P/Russell 3	JFC	2.62	0.329	14.1	14
99P/Kowal 1	JFC	4.74	0.229	4.33	17
121P/Shoemaker-Holt 2	JFC	3.75	0.185	20.2	4
127P/Holt-Olmstead	JFC	2.19	0.363	14.3	2
139P/Vaisala-Oterma	JFC	3.40	0.247	2.33	9
140P/Bowell-Skiff	JFC	1.97	0.692	3.84	21.5
142P/Ge-Wang	JFC	2.49	0.498	12.3	4.67
158P/Kowal-LINEAR	JFC	4.59	0.0287	7.91	4
189P/NEAT	JFC	1.18	0.597	20.4	2
195P/Hill	JFC	4.44	0.315	36.4	2
206P/Barnard-Boattini	JFC	0.979	0.689	32.0	1
226P/Pigott-LINEAR-Kowalski	JFC	1.92	0.480	46.3	3
249P/LINEAR	JFC	0.511	0.816	8.43	4
254P/McNaught	JFC	3.21	0.312	32.6	1
269P/Jedicke	JFC	4.07	0.435	6.61	1
318P/McNaught-Hartley	JFC	2.48	0.671	17.6	10
C/1999 XS87 (LINEAR)	JFC	2.77	0.841	14.8	3
C/2001 M10 (NEAT)	JFC	5.30	0.801	28.1	2
C/2002 A1 (LINEAR)	JFC	4.71	0.725	14.1	4
P/2002 T5 (LINEAR)	JFC	3.93	0.437	30.9	3
C/2003 E1 (NEAT)	JFC	3.24	0.764	33.5	1
P/2004 A1 (LONEOS)	JFC	5.46	0.308	10.6	7
P/2004 V3 (Siding Spring)	JFC	3.94	0.446	50.5	2
C/2007 S2 (Lemmon)	JFC	5.56	0.557	16.9	2
C/2008 E1 (Catalina)	JFC	4.83	0.548	35.0	1
P/2008 O3 (Boattini)	JFC	2.50	0.695	32.3	2
P/2010 H2 (Vales)	JFC	3.11	0.193	14.3	1
P/2010 H5 (Scotti)	JFC	6.03	0.156	14.1	1
C/2011 KP36 (Spacewatch)	JFC	4.88	0.873	19.0	1

Table 3.1 (cont'd)

Name	Orbital type[a]	q^b [au]	e^c	i^d [°]	w_i^e
P/2012 C3 (PANSTARRS)	JFC	3.62	0.626	9.19	9
C/2012 Q1 (Kowalski)	JFC	9.48	0.637	45.2	1
P/2012 US27 (Siding Spring)	JFC	1.82	0.649	39.3	1
C/2012 X2 (PANSTARRS)	JFC	4.75	0.771	34.1	1
P/2013 EW90 (Tenagra)	JFC	3.30	0.196	31.8	1
2003EH1	JFC	1.19	0.618	70.8	1
74P/Smirnova-Chernykh	ETC-1	3.54	0.149	6.65	5
87P/Bus	ETC-1	2.10	0.389	2.60	8
94P/Russell 4	ETC-1	2.23	0.364	6.18	6
2P/Encke	ETC-2	0.336	0.848	11.8	1
233P/La Sagra	ETC-2	1.79	0.409	11.3	5
259P/Garradd	ETC-2	1.79	0.342	15.9	1
311P/PANSTARRS	ETC-2	1.94	0.115	4.97	2
324P/La Sagra	ETC-2	2.62	0.154	21.4	1
331P/Gibbs	ETC-2	2.88	0.0414	9.74	1
39P/Oterma	CTC	5.47	0.246	1.94	2
165P/LINEAR	CTC	6.83	0.622	15.9	1
166P/NEAT	CTC	8.56	0.383	15.4	2
167P/CINEOS	CTC	11.8	0.270	19.1	1
P/2005 S2 (Skiff)	CTC	6.40	0.197	3.14	2
C/2013 C2 (Tenagra)	CTC	9.13	0.429	21.3	2
1P/Halley	HTC-1	0.586	0.967	162.	3
8P/Tuttle	HTC-1	1.03	0.820	55.0	1
12P/Pons-Brooks	HTC-1	0.774	0.955	74.2	2
13P/Olbers	HTC-1	1.18	0.930	44.6	4
23P/Brorsen-Metcalf	HTC-1	0.479	0.972	19.3	2
27P/Crommelin	HTC-1	0.748	0.919	29.0	4
35P/Herschel-Rigollet	HTC-1	0.748	0.974	64.2	5
55P/Tempel-Tuttle	HTC-1	0.976	0.906	162.	2

Table 3.1 (cont'd)

Name	Orbital type[a]	q^b [au]	e^c	i^d [°]	w_i^e
109P/Swift-Tuttle	HTC-1	0.960	0.963	113.	1
122P/de Vico	HTC-1	0.659	0.963	85.4	2
126P/IRAS	HTC-1	1.72	0.696	45.8	1
161P/Hartley-IRAS	HTC-1	1.27	0.835	95.7	1
177P/Barnard	HTC-1	1.11	0.955	31.2	3
262P/McNaught-Russell	HTC-1	1.28	0.815	29.1	1
273P/Pons-Gambart	HTC-1	0.810	0.975	136.	2
C/1855 L1 (Donati)	HTC-1	0.568	0.986	157.	1
C/1857 O1 (Peters)	HTC-1	0.747	0.980	32.8	3
C/1906 V1 (Thiele)	HTC-1	1.21	0.949	56.0	2
C/1921 H1 (Dubiago)	HTC-1	1.10	0.848	22.1	1
C/1937 D1 (Wilk)	HTC-1	0.619	0.981	26.0	2
C/1998 G1 (LINEAR)	HTC-1	2.13	0.824	110.	2
C/1998 Y1 (LINEAR)	HTC-1	1.75	0.924	28.1	1
C/1999 E1 (Li)	HTC-1	3.92	0.760	46.9	1
C/1999 K4 (LINEAR)	HTC-1	1.44	0.915	121.	1
C/2001 OG108 (LONEOS)	HTC-1	0.994	0.925	80.2	1
P/2001 Q6 (NEAT)	HTC-1	1.41	0.824	56.9	2
C/2001 W2 (BATTERS)	HTC-1	1.05	0.941	116.	3
C/2002 B1 (LINEAR)	HTC-1	2.27	0.771	51.0	1
C/2002 CE10 (LINEAR)	HTC-1	2.05	0.791	145.	1
C/2003 F1 (LINEAR)	HTC-1	4.01	0.806	70.2	1
C/2003 H2 (LINEAR)	HTC-1	2.18	0.943	74.2	1
C/2003 R1 (LINEAR)	HTC-1	2.10	0.893	149.	2
C/2003 U1 (LINEAR)	HTC-1	1.80	0.922	164.	1
C/2005 N5 (Catalina)	HTC-1	1.63	0.943	21.4	1
P/2006 R1 (Siding Spring)	HTC-1	1.67	0.702	160.	1
P/2010 D2 (WISE)	HTC-1	3.66	0.453	57.2	1
P/2010 JC81 (WISE)	HTC-1	1.81	0.777	38.7	1

Table 3.1 (cont'd)

Name	Orbital type[a]	q^b [au]	e^c	i^d [°]	w_i^e
C/2010 L5 (WISE)	HTC-1	0.791	0.904	147.	1
C/2011 J3 (LINEAR)	HTC-1	1.45	0.926	115.	1
C/2011 L1 (McNaught)	HTC-1	2.24	0.797	65.5	1
P/2012 NJ (La Sagra)	HTC-1	1.29	0.848	84.4	1
P/2013 AL76 (Catalina)	HTC-1	2.05	0.685	145.	1
C/2013 V3 (Nevski)	HTC-1	1.39	0.891	32.1	1
C/2014 W10 (PANSTARRS)	HTC-1	7.42	0.604	73.0	1
P/2015 A3 (PANSTARRS)	HTC-1	1.15	0.848	173.	2
96P/Machholz 1	HTC-2	0.124	0.959	58.3	1
P/1999 J6 (SOHO)	HTC-2	0.0491	0.984	26.6	5

[a]Orbital types of comets (see subsection 3.2.2)

[b]Perihelion distance

[c]Eccentricity

[d]Inclination

[e]Initial weighting factor (see subsection 3.2.2)

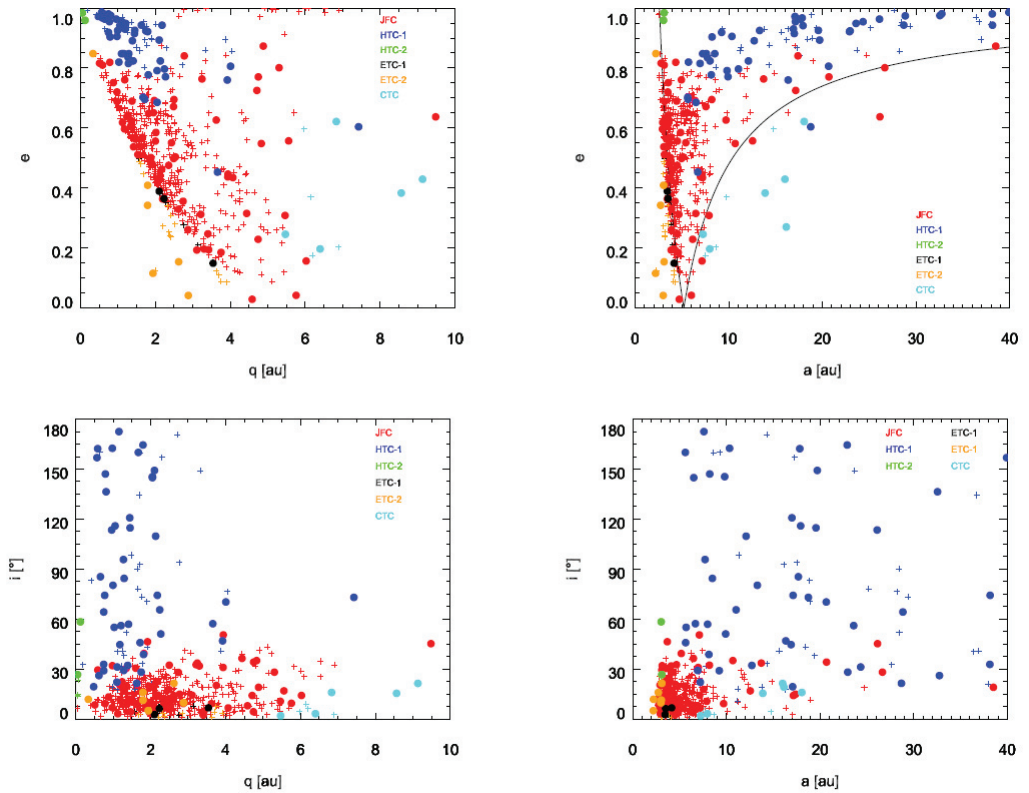

Figure 3.1. Orbital element distributions of all comets with semimajor axes shorter than 40 au, discovered before 2015 January 23. Large filled circles are comets included in our numerical integration, and small crosses are comets that are not included.

3.2.3 Dust ejection

We ejected dust particles from the orbits of the above actual cometary nuclei through the following methods. At first, the orbits of comets at the epoch t_0 = JD 2457054.5 were numerically calculated from the orbital elements of the JPL Horizons comet lists. Then, five orbital elements of the comets were fixed, except for anomalies. All dust particles were ejected simultaneously at the epoch on the orbits of comets with randomized true anomalies. We ejected 100 dust particles per given size per cometary orbit for particles with $\beta \leq 0.00285$ and 50 for particles with $\beta \geq 0.00114$.

We distributed the true anomalies as the number density of ejected dust particles becomes a function of heliocentric distance following the observed dust ejection efficiency change (Ishiguro et al. 2007; Mazzotta Epifani et al. 2009; Hanayama et al. 2012). Where $N(r_{\rm h})$ denotes the initial number density of ejected particles on the given cometary orbit

in cm^{-3}, and r_h denotes the heliocentric distance in au, we distributed the particles as:

$$N(r_\mathrm{h}) \propto r_\mathrm{h}^{-3.0} \quad , \tag{3.3}$$

The ejection velocities $v_{ej}(r_\mathrm{h})$ are given as their directions are randomly distributed over the sunlit hemisphere following an uniform probability distribution, and their speeds are given as a function of β and r_h (Ishiguro et al. 2007; Hanayama et al. 2012):

$$v_{ej}(r_\mathrm{h}) = 200[\mathrm{m\ s}^{-1}]\beta^{0.5} r_\mathrm{h}^{-0.5} \quad , \tag{3.4}$$

Although we assumed a relatively realistic situation in ejecting dust particles compared to the cases with zero ejection velocity, the added ejection velocities numerically function as a kind of cloning process because the ejection velocities are small compared to the orbital velocities. Likewise, even though we ejected dust particles simultaneously at different positions on the cometary orbits instead of the exact position of nuclei at the epoch, dynamically, this approach is the same as changing the anomaly without changing other orbital elements, and therefore, this method works as if it were a cloning process.

The initial orbital elements of ejected dust particles were calculated after the ejection velocities were added to the orbital velocities, taking account of the change of orbital elements due to radiative acceleration.

3.2.4 IDP complex modeling

We assumed that all of the above cometary nuclei eject dust particles at the same rate when we calculate the average over single revolutions. We also assumed that all nuclei eject dust particles with same shape and SFD once we fixed these parameters. Under these assumptions, the ratio between initial dust masses JFCs : HTC-2 : ETC-1 : ETC-2 is 486 : 6 : 19 : 11.

We constructed an IDP distribution covering different ages of particles for given β values using the following methods. First, we recorded the positions and velocities of dust particles every 100 years and cloned $1000 \times w_i$ particles from the each individual dust particle. We set the number of the clones to be proportional to the parameter w_i. During the cloning process, we kept three orbital elements (i.e., the semimajor axes, eccentricities and inclinations) constant and randomized their arguments of perihelion, longitudes of ascending node, and mean anomalies for each clone. Consequently, we made snapshots composed of clones with single β values and from the same class of

cometary population every 100 years. Assuming a steady state, (i.e., that dust ejections have occurred constantly over two million years), we regarded dust particle records after a given time of integration from the current epoch as records from possible ejections at the same amount of time before the current epoch. This assumption is similar with that made in previous works such as Wiegert et al. (2009). Finally, the snapshots were summed together, constructing an IDP distribution covering the full dynamical evolution from sources to sinks.

Using the above information from our numerical calculation, we validated the initial dust ejection conditions through following methods. Whenever the initial conditions about dust particle shape, mass density and initial SFD were given, the resulting IDP cloud complex models were derived. We constructed a three–dimensional grid in Cartesian coordinates. 0.1 au $\times$ 0.1 au $\times$ 0.1 au grids were constructed throughout interplanetary space, and the number of dust particles of a given β value within a single grid were counted. The results of different β values were weighted by the given initial conditions (see subsection 3.3.2). As a next step, we derived the cumulative number, cross-section and mass distribution of IDPs in the grid box, assuming a piecewise exponential SFD within every single grid box. Then, after summing the numbers from different source populations, the resulting SFDs around the Earth's orbit were normalized at $\beta = 0.00285$ and compared with the observational SFD in Grün et al. (1985), which was obtained through the *Pegasus* and *HEOS-2* missions and widely applied as the reference SFD model. We examined the ratio between our normalized SFD and the observed one between β of $0.00057 \sim 0.114$ and treat the given initial conditions as valid if the ratio in SFD is between $0.5 \sim 2$ for every β value. For such cases, we derived a goodness-of-fit as the averaged absolute values of the logarithm of the ratios.

Finally, the total IDP cloud complex model was scaled to match the observed zodiacal light brightness in the anti-solar direction (i.e., gegenschein) (Leinert et al. 1998; Ishiguro et al. 2013). As we mentioned in subsection 3.2.1, we limited the largest dust size to $\beta = 0.00057$. This cut-off is expected to have negligible effects on the total cross-section but may exert a considerable influence on the total mass according to the initial conditions. Therefore, we tabulated the total mass supply in two cases, namely up to $\beta \geq 0.00114$ and $\beta \geq 0.00057$, along with validated initial conditions.

3.3 Results

3.3.1 Orbital evolution of dust particles according to different source populations and sizes

In this chapter, the sinks of dust particles were determined by close encounters with planets for the most cases. We will explain the role of close encounter, which concurs with previous research. Dust particles ejected from comets fall to the Sun because of P–R drag if the solar gravity and radiation of the Sun are the only two factors affecting their orbits. P–R drag continuously reduces the a and e of the dust particles. The effect of resonances with planets (i.e., the mean motion and secular resonances) themselves do not change sinks of dust particles significantly because the resonances change e rather than a. Note that the lifetime of dust particles may be changed by resonances, which would increase the lifetime of dust particles temporarily by trapping them. In contrast, close encounters with planets, mainly Jupiter, can completely change the orbits of dust particles and usually prevent falls of the dust particles to the Sun. As a consequence of close encounters, a may decrease or increase, and any e value may occur from a circular orbit to a hyperbolic orbit. Dust particles ejected from the JFCs are prone to close encounters with Jupiter because the initial orbits of their source comets intersect or are close to the Jovian orbit and have slow relative velocities to Jupiter.

Smaller dust particles have higher chances of avoiding close encounters than larger particles because they fall to the Sun faster via P–R drag and therefore reside for a shorter period of time in the region where the Jovian gravity is critical. Figure 3.2 shows the lifetime of dust particles under radiative acceleration. For comparison, we construct the lifetime in the case where there are no planetary perturbations. Because P–R drift is slow for large particles, the lifetime of particles that are larger than 100 μm is determined by close encounter, not by P–R drift. Therefore, the lifetimes of large dust particles are similar to those of their parent bodies, $\sim 100 - 300$ thousands years ($\sim$ 100 thousands years in weighted median, $\sim$ 250 thousands years in weighted average) (Levison & Duncan 1994, 1997). Note that the lifetime with planetary perturbation included the effects of resonances. The resonances may increase the lifetime of dust particles by temporarily trapping them, especially for the particles which have evolved into the inner solar system. The dust number density derived from this work are given in Figure 3.3, according to particle size.

We measured the fraction of dust particles transferred into the inner solar system ($a \leq 1$ au) for different populations with different sizes (Table 3.2). The probability of successful transfer to an orbit with a semimajor axis smaller than 1 au will be selectively

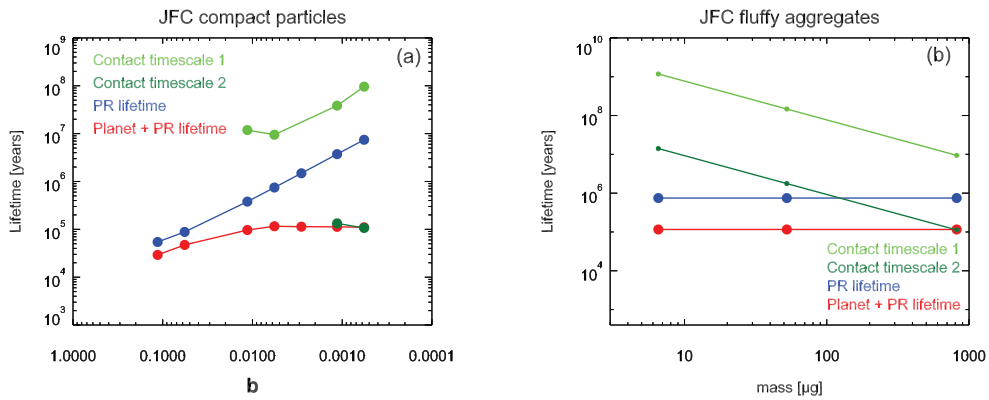

Figure 3.2. Dynamical lifetime, P–R lifetime and contact timescale of cometary dust particles. The values here are the weighted median of all dust particles. Dynamical and P–R lifetimes were calculated by numerical integration of dust particles both with and without planetary gravities. When there are no planets, we integrated the orbits of dust particles until they fall to the Sun without limit. (a) Contact timescales are calculated based on the values in the first line of Table 3.7. Contact timescale 1 is the timescale required for contact with a projectile 10 times smaller than the particle in diameter, and contact timescale 2 is the value for a projectile 100 times smaller. Impact velocities are not considered. (b) P–R lifetimes of fluffy aggregates are independent from mass, as explained in subsection 3.3.2. Contact timescales are calculated using the values in the first line of Table 3.8. Contact timescale 1 is the timescale required for contact with a projectile with a 125 μm or larger diameter, and contact timescale 2 is the value for projectile with a 25 μm or larger diameter.

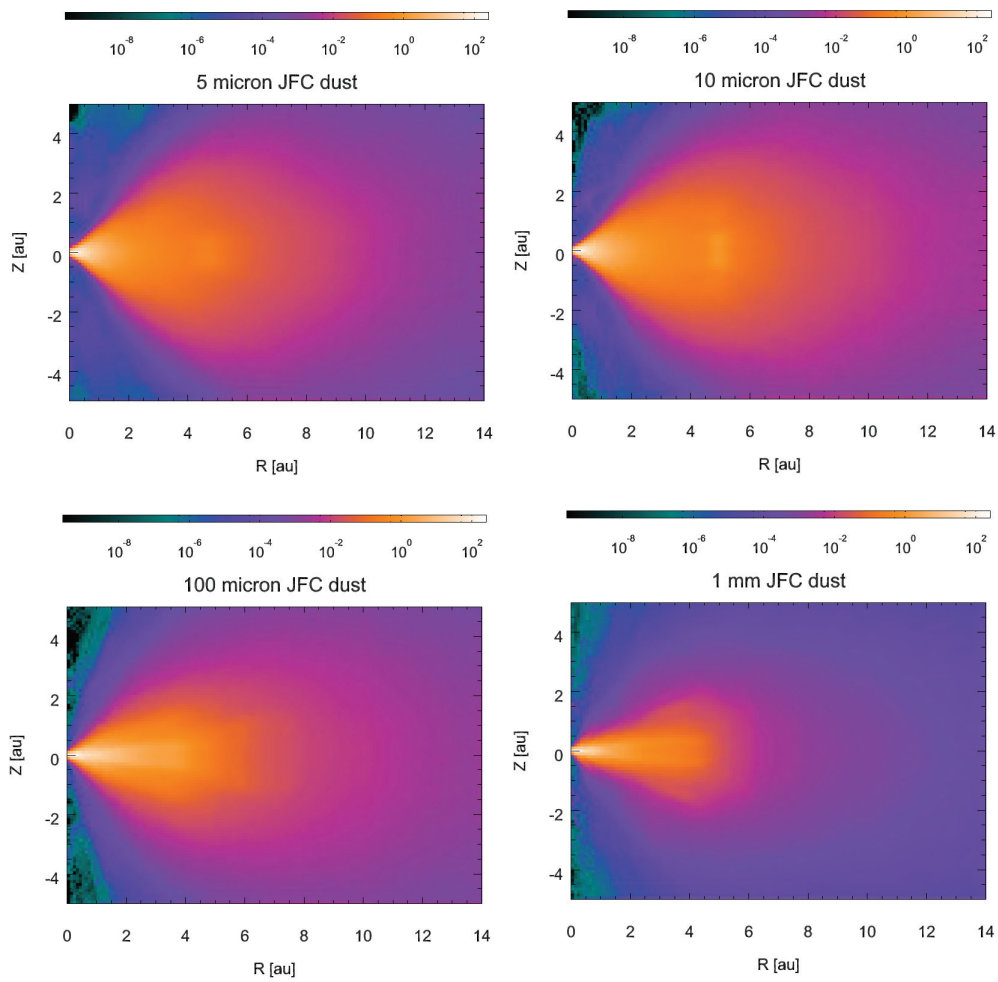

Figure 3.3. Number density distributions according to different particle sizes. The distribution of 5, 10, 100, and 1000 μm particles from JFCs are drawn. The unit of these figures is arbitrary but normalized to the amount of initial dust number of the size. The Sun is positioned at the left center of each image.

higher for dust particles meeting the following two conditions: dust particles ejected from objects the aphelion distances of which are shorter than the semimajor axis of Jupiter and that are free from close encounters with Jupiter, ETC-2s and asteroids; and dust particles that are small. We checked that the dust particles that are not transferred to the inner solar system within 2 million years of integration time satisfy one of the following conditions: trapped in the Trojan region; or $\beta < 0.00114$ and free from planetary encounter and thus still under P–R decay. The latter case includes dust particles ejected from AAs and asteroids, and we performed 5 million years of integration for these particles to complete the dust particle evolution process. The proportions of surviving dust particles after two million years of integration are summarized in Table 3.3.

Table 3.2. Proportion of dust particles with $a \leq 1$ AU from different source populations and β values [%].

β	0.57	0.285	0.114	0.057	0.0114	0.0057	0.00285	0.00114	0.00057
JFC	0.025	4.3	41	45	30	25	16	5.6	2.9
ETC-1	0.0	9.8	47	30	19	12	6.9	2.6	0.84
ETC-2	0.0	25	73	77	97	99	100	100	97
HTC-1	0.0	0.22	3.2	13	19	12	5.5	1.4	0.16
HTC-2	0.0	0.0	0.0	0.0	0.83	1.0	0.0	0.33	0.0
CTC	0.0	0.30	7.2	12	8.1	5.2	3.1	0.80	0.0
Asteroids	0.052	35	86	94	97	96	96	87	6.5

Table 3.3. Proportion of dust particles that remain in the solar system after 2 million years of integration [%].

β	0.57	0.285	0.114	0.057	0.0114	0.0057	0.00285	0.00114	0.00057
JFC	0.0	0.0	0.0	0.025	0.75	1.1	1.6	1.8	2.6
ETC-1	0.0	0.0	0.0	0.0	2.4	0.89	1.9	2.6	3.8
ETC-2	0.0	0.0	0.0	0.0	0.0	0.0	0.0	8.7	57
HTC-1	0.0	0.0	0.0	0.0	0.99	1.6	2.3	4.0	4.7
HTC-2	0.0	0.0	0.0	0.0	0.0	0.0	0.0	0.0	0.0
CTC	0.0	0.0	0.80	3.3	8.7	8.2	9.8	7.6	10
Asteroids	0.0	0.0	0.0	0.10	0.16	0.0	0.21	6.8	84

3.3.2 Effects of dust particle shape, density and SFD

In previous subsection, we explained the different evolutionary tracks between the particles with different β values. From now on, we will connect the dust SFD measured around the Earth's orbit with that measured around cometary comae.

According to measurements of the *Rosetta* mission, the dust SFD at coma of 67P/Churyumov-Gerasimenko changed over time, but it appears that there are at least two bending points in SFD that can thus be approximated by a doubly broken power-law function. The bending points were determined at $\sim 10^{-6}$g and $\sim 10^{-4}$g for most cases except for the region around perihelion (Rotundi et al. 2015; Hilchenbach et al. 2016; Fulle et al. 2016a; Agarwal et al. 2016; Merouane et al. 2016). The power law exponents α for differential mass distributions $dn \propto m^{-\alpha} dm$ varied between $\sim 1.75-2.05$ for the smallest masses, $\sim 0.97-1.67$ for intermediate masses (~ 1.9 right after perihelion), and at approximately ~ 2.0 for largest masses. The results from the *Stardust* mission (Green et al. 2004, 2007), *Giotto* mission (Fulle et al. 1995), and IR observation (Vaubaillon & Reach 2010) coincided with this point. This distribution is different from that measured around the Earth's orbit by the *Pegasus* and *HEOS-2* missions (Grün et al. 1985), but the difference itself is understandable when we consider the content of the previous subsection.

As explained before, what we actually calculated were orbital evolutionary tracks as a function of initial orbits and β values. In this subsection, at first, we converted β to particle mass assuming particle shape and density. Next, we found the expected initial dust SFD that can explain the measured SFD around the Earth's orbit. Finally, we compared the expected initial dust SFD with the measured one and derived adequate assumptions.

Cometary dust particles have been conventionally approximated as having a compact structure and an spherical shape. For compact particles, a low mass density of 0.8 g cm^{-3} was derived from modeling porous icy dust via the *Rosetta* measurements (Fulle et al. 2016b), but a relatively wide density range of 1.9 ± 1.1 g cm^{-3} was measured during the *Rosetta* mission by direct comparison between cross–section and impact momenta assuming particle shape (Rotundi et al. 2015). We thus tested the three different values of particle mass densities, namely 0.8 g cm^{-3}, 1.9 g cm^{-3}, and 3.0 g cm^{-3} (Rotundi et al. 2015; Fulle et al. 2016b).

Despite the conventional treatment of IDPs as compact spherical particles, large fluffy aggregates (larger than hundreds of micrometers in diameter) were recently found around 67P/Churyumov-Gerasimenko via the observations of the *Rosetta* spacecraft

(Fulle et al. 2015; Bentley et al. 2016; Mannel et al. 2016). Although the detailed physical properties such as the structures and/or porosity of the fluffy aggregates are not well-investigated, it is likely that these fluffy aggregates have mass densities as low as 0.001 g cm^{-3} (Fulle et al. 2015), and fractal dimensions were estimated to be 1.87 (Fulle et al. 2015; Mannel et al. 2016). Under these conditions, the cross-section to mass ratio of the aggregates is expected to be constant regardless of aggregate mass, or at least exhibits only insignificant changes unlike the compact particles (Mukai et al. 1992; Skorov et al. 2016). We are not sure about the exact cause of the shallow SFD between $10^{-6} - 10^{-4}$ g, but we conjecture that the fluffy aggregates that were discovered by the *Rosetta* mission (Fulle et al. 2015; Bentley et al. 2016; Mannel et al. 2016) are responsible for this shallow SFD slope. The time of the change in the fluffy aggregate ratio coincides with change in SFD around perihelion (Della Corte et al. 2015, 2016), and the size of large fracta from fluffy aggregates match the particle size of the smaller bending point in the SFD (Hilchenbach et al. 2016; Merouane et al. 2016).

As the first trial, we employed the initial SFD of compact spherical dust particles with a single power law. Where dn is the differential number density of dust particles of mass m, the initial SFD is written as $dn \propto m^{-\alpha} dm$. We tested different α values with intervals of 1/12. In this model, we cannot validate any initial parameters that yields less than two times the difference between observations and expectations; therefore, we tabulated the initial parameters, yielding results that are less than five times different from the observation. The derived power index, α, is summarized in Table 3.4. We also show the results of the fitting in Figure 3.4 along with other cases. We present the ratio between our best-fit SFD and that of Grün et al. (1985) in Figure 3.5.

Table 3.4. Best-fit parameters and expected mass supply rate for the SFD model 1[a]

ρ [g cm^{-3}]	α	$dm_{\rm total}/dt$ [t s^{-1}][b]	$dm_{\rm total}/dt$ [t s^{-1}][c]	goodness of fit [d]
0.8	2.000 − 2.167	39 − 45	35 − 43	0.22 − 0.32
1.9	1.917 − 2.000	39 − 44	∼35	0.27
3.0	1.833 − 2.000	44 − 53	35 − 37	0.25 − 0.27

[a] $dn \propto m^{-\alpha} dm$

[b] Total mass supply rate into the IDP cloud complex for particles with $\beta > 0.00057$

[c] Total mass supply rate into the IDP cloud complex for particles with $\beta > 0.00114$

[d] Average of absolute values of log of ratio between our model and observed model (Grün et al. 1985)

Second, we employed compact spherical dust particles having a broken power-law initial SFD, namely $dn \propto m^{-\alpha_1} dm$ for $m \leq m_c$ and $dn \propto m^{-\alpha_2} dm$ for $m \geq m_c$. When fitting the data, we changed m_c between 5 discrete β values included in the numerical integration. The derived initial parameters are tabulated in Table 3.5.

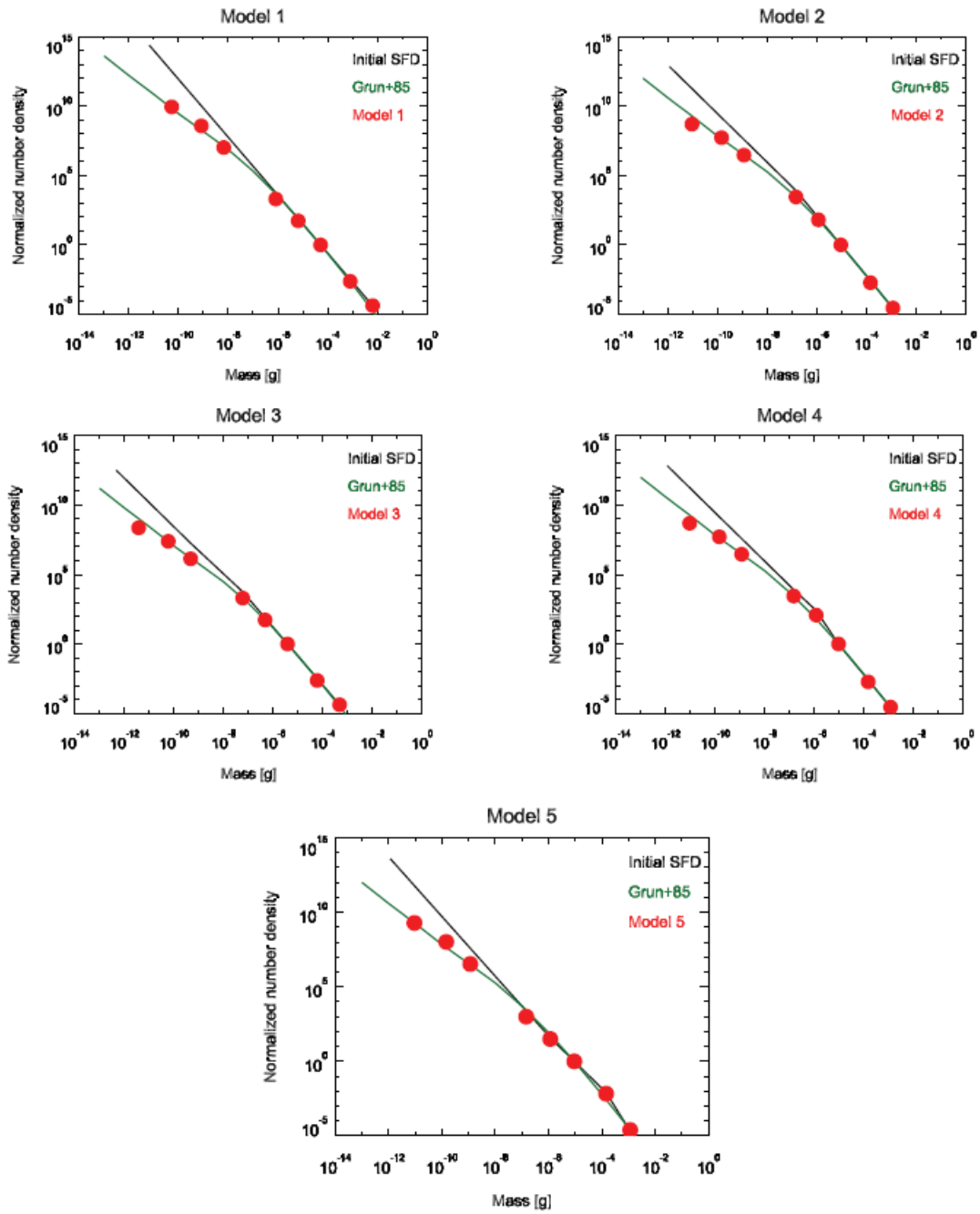

Figure 3.4. Comparison of SFDs between the observation and our models. Black lines are initial SFD at the source regions calculated from the model parameters tabulated in Table 3.4–3.8. The best-fit values are used in drawing solid lines. Green lines are observed SFD around the Earth's orbit via *Pegasus* and *HEOS-2* spacecrafts. Red dots are SFD around the Earth's orbit derived from our models using the best fit parameters or parameters measured around cometary nuclei by *Rosetta* and *Stardust* missions for model 5.

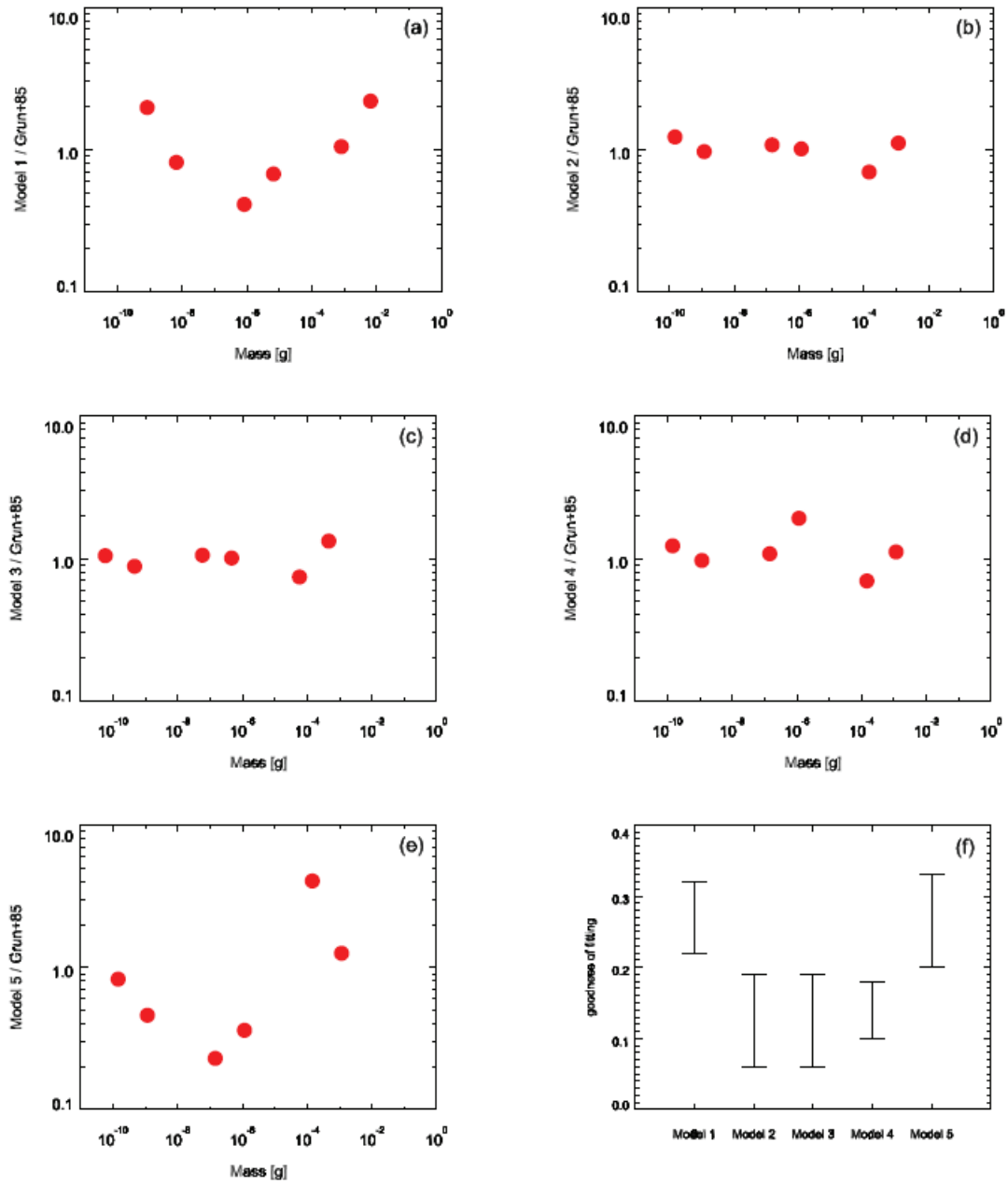

Figure 3.5. Ratio between our best-fit SFD models and observed SFD around the Earth's orbit by *Pegasus* and *HEOS-2* spacecraft. Figure (e) is not from best-fit input parameters but from parameters measured around cometary nuclei by *Rosetta* and *Stardust* missions. (f) Goodness of fit indicates the average of absolute values of the log of the ratio between the model with the parameter and the observed model from (Grün et al. 1985).

Table 3.5. Best-fit parameters and expected mass supply rate for the SFD model 2[a]

ρ [g cm^{-3}]	m_c [g]	α_1	α_2	$dm_{\rm total}/dt$ [t s^{-1}][b]	$dm_{\rm total}/dt$ [t s^{-1}][c]	goodness of fit [d]
0.8	6.5×10^{-9}	1.583 − 1.667	2.167	∼29	∼28	0.16 − 0.18
0.8	8.2×10^{-7}	1.833 − 2.000	2.167 − 2.333	30 − 35	30 − 34	0.09 − 0.15
0.8	6.5×10^{-6}	2.000	2.333	∼34	∼34	0.18
1.9	1.4×10^{-7}	1.583 − 1.833	2.083 − 2.250	31 − 36	30 − 32	0.06 − 0.19
1.9	1.2×10^{-6}	1.833 − 1.917	2.083 − 2.250	34 − 37	32 − 34	0.11 − 0.16
3.0	5.8×10^{-8}	1.583 − 1.833	2.000 − 2.167	34 − 41	31 − 34	0.06 − 0.16
3.0	4.7×10^{-7}	1.750 − 1.833	2.000 − 2.167	36 − 42	33 − 35	0.11 − 0.15

[a] $dn \propto m^{-\alpha_1} dm$ for $m \leq m_c$, and $dn \propto m^{-\alpha_2} dm$ for $m \geq m_c$

[b] Total mass supply rate into the IDP cloud complex for particles with $\beta > 0.00057$

[c] Total mass supply rate into the IDP cloud complex for particles with $\beta > 0.00114$

[d] Average of absolute values of log of ratio between our model and observed model (Grün et al. 1985)

Third, we tested the case of a doubly broken power-law SFD with compact spherical dust particles. SFD was assumed with the form of $dn \propto m^{-\alpha_1} dm$ for $m \leq m_{c1}$, $dn \propto m^{-\alpha_2} dm$ for $m_{c1} \leq m \leq m_{c2}$ and $dn \propto m^{-\alpha_3} dm$ for $m_{c2} \leq m$. In this case, we assumed $\alpha_1 > \alpha_2$, $\alpha_3 > \alpha_2$ and limited parameters as in the previous case. The results are tabulated in Table 3.6.

Table 3.6. Best-fit parameters and expected mass supply rate for the SFD model 3[a]

ρ [g cm^{-3}]	m_{c1} [g]	m_{c2} [g]	α_1	α_2	α_3	$dm_{\rm total}/dt$[b] [t s^{-1}]	$dm_{\rm total}/dt$[c] [t s^{-1}]	goodness of fit [d]
0.8	6.5×10^{-9}	$8.2\times10^{-7} - 6.5\times10^{-6}$	1.917 − 2.250	1.833 − 2.000	2.167 − 2.333	31 − 46	31 − 45	0.10 − 0.19
1.9	$6.5\times10^{-9} - 8.2\times10^{-7}$	$8.2\times10^{-7} - 6.5\times10^{-6}$	1.667 − 2.167	1.583 − 1.833	2.083 − 2.250	32 − 39	30 − 36	0.07 − 0.19
3.0	$6.5\times10^{-9} - 8.2\times10^{-7}$	$8.2\times10^{-7} - 6.5\times10^{-6}$	1.667 − 2.250	1.583 − 1.833	2.000 − 2.167	34 − 44	31 − 38	0.06 − 0.16

[a] $dn \propto m^{-\alpha_1} dm$ for $m \leq m_{c1}$, $dn \propto m^{-\alpha_2} dm$ for $m_{c1} \leq m \leq m_{c2}$ and $dn \propto m^{-\alpha_3} dm$ for $m_{c2} \leq m$

[b] total mass supply rate into the IDP cloud complex by particles with $\beta > 0.00057$

[c] total mass supply rate into the IDP cloud complex by particles with $\beta > 0.00114$

[d] average of absolute values of log of ratio between our model and observed model (Grün et al. 1985)

The next model is composed of both compact spherical particles and fluffy aggregates. We assumed that the fluffy aggregates have constant β values regardless of mass (Mukai et al. 1992; Skorov et al. 2016). The SFD of compact spherical particles was assumed to be $dn \propto m^{-\alpha_1} dm$ for $m \leq m_{c_1}$ and $dn \propto m^{-\alpha_3} dm$ for $m \geq m_{c_1}$. The SFD of fluffy aggregates was assumed to be the sum of fluffy aggregates, and compact spherical particles become $dn \propto m^{-\alpha_2} dm$ between masses of m_{c_1} and m_{c_2}. The results are presented in Table 3.7.

Table 3.7. Best-fit parameters, expected mass supply rate and contribution of fluffy particles in zodiacal light for the SFD model 4[a]

ρ [g cm^{-3}]	m_{c1} [g]	m_{c2} [g]	α_1	α_2	α_3	$dm_{\rm comp}/dt$[b] [t s^{-1}]	$dm_{\rm fluf}/dt$[c] [t s^{-1}]	$ZL_{\rm fluf}/ZL$[d]	$m_{\rm fluf}/m_{\rm total}$[e]	goodness of fit[f]
0.8	8.2×10^{-7}	6.5×10^{-6}	1.917−2.000	1.583−1.917	2.167−2.250	32−35	0.05−0.2	0.005	0.003−0.007	0.12−0.18
1.9	1.5×10^{-7}	1.2×10^{-6}	1.750−1.833	1.583−1.750	2.083−2.167	33−36	0.1−0.3	0.008	0.004−0.006	0.10−0.14
3.0	5.8×10^{-8}	4.7×10^{-7}	1.667−1.833	1.583−1.750	2.000−2.083	36−41	0.1−0.3	0.007	0.002−0.006	0.10−0.17

[a]Explanations of functional form in text

[b]Total mass supply rate into the IDP cloud complex for compact particles

[c]Total mass supply rate into the IDP cloud complex for fluffy aggregates

[d]Fraction of gegenschein brightness contributed by fluffy aggregates

[e]Fraction of fluffy aggregates mass around the Earth's orbit

[f]Average of absolute values of log of ratio between our model and observed model (Grün et al. 1985)

The best-fit initial SFD of previous paragraph has bending points at smaller mass than SFD measured at cometary comae, and the slopes steeper than measurements in $0.0057 < \beta < 0.000114$ (Table 3.7). As a final model, we applied SFD with the same functional form as that in the above model but fixed m_{c1} and m_{c2} around the observed values. Then, the α_1, α_2, and α_3 values will be near the observed values, especially when compact particle density is higher than 1.9 g cm^{-3}. In those cases, the ratio between our estimation and Grün et al. (1985)'s model worsened by a factor of three for some sizes. However, our model using this observed input parameter value is still not far from the observed SFD in the Earth's orbit as presented in Table 3.8 and Figures 3.3 and 3.4.

Table 3.8. Best-fit parameters, expected mass supply rate and contribution of fluffy particles in zodiacal light for model 5[a]

ρ [g cm^{-3}]	m_{c1} [g]	m_{c2} [g]	α_1	α_2	α_3	$dm_{\rm comp}/dt$[b] [t s^{-1}]	$dm_{\rm fluf}/dt$[c] [t s^{-1}]	$ZL_{\rm fluf}/ZL$[d]	$m_{\rm fluf}/m_{\rm total}$[e]	goodness of fit[f]
0.8	6.5×10^{-6}	8.2×10^{-4}	2.083−2.167	1.833−2.000	2.083−2.250	34−41	0.8−3	0.07	0.12−0.25	0.20−0.33
1.9	1.2×10^{-6}	1.5×10^{-4}	1.917−2.000	1.583−1.750	1.917−2.250	25−36	4−8	0.20	0.17−0.37	0.21−0.33
3.0	3.7×10^{-6}	5.8×10^{-5}	1.833−1.917	1.667−1.833	1.917−2.333	35−48	0.06−0.5	0.007	0.17−0.44	0.20−0.31

[a]Explanations of functional form in text

[b]Total mass supply rate into the IDP cloud complex for compact particles

[c]Total mass supply rate into the IDP cloud complex for fluffy aggregates

[d]Fraction of gegenschein brightness caused by fluffy aggregates

[e]Fraction of fluffy aggregates mass around the Earth's orbit

[f]Average of absolute values of log of ratio between our model and observed model (Grün et al. 1985)

As presented in Figure 3.5 and Tables 3.4–3.8, different dust ejection conditions for dust particle shape and density can be validated with the appropriate initial SFD. It is noteworthy that the dust ejection conditions measured around 67P/Churyumov-Gerasimenko and 81P/Wild 2 concur with dust particle measurements around the Earth's orbit when we assume the existence of fluffy aggregates of discovered size range. We consider that the various dust environments measured around cometary nuclei are in accordance with our knowledge about the IDP cloud complex and its cometary origin and that the target comets of space missions (i.e., 1P, 67P, and 81P) are not extraordinary but may represent ordinary dust ejections from comets.

3.3.3 Mass supply rate to the IDP cloud complex

By scaling our model SFD by the observed gegenschein brightness, we calculated the expected mass supply rate to the IDP cloud complex. As presented in Tables 3.4–3.8 and Figure 3.6, the total dust supply rate does not vary greatly according to dust particle shape, density and the initial SFD when the latter is confined by the observed SFD around the Earth's orbit and gegenschein brightness. The required dust supply rate for particles with $\beta > 0.00057$ was 39−45 tons s^{-1} for model 1, 29−41 tons s^{-1} for model 2, 31−49 tons s^{-1} for model 3, 32− 41 tons s^{-1} for model 4, and 32−43 tons s^{-1} for model 5. We thus find that the different SFD models in this research do not significantly change the mass supply rate. This value is roughly consistent with but slightly larger than Nesvorný et al. (2011)'s estimation of 1.6−25 tons s^{-1}. When we consider that our derived SFD is shallower than Nesvorný et al. (2011)'s, we believe that this difference is understandable.

Even though we did not include dust particles larger than $\beta = 0.00057$, we expect that this omission will not critically change our conclusion because the mass supply rates for $\beta \geq 0.00114$ and $\beta \geq 0.00057$ are not significantly different from each other, as shown in Tables 3.4–3.8.

3.3.4 The Mutual collisions

Collisional probabilities of the solar system objects have been investigated since the pioneering works by Opik (1951) and Dohnanyi (1969). Collisional lifetime of IDPs was estimated under the assumption of the fixed circular orbits (Dohnanyi 1978; Grün et al. 1985; Steel & Elford 1986). It is noticed that catastrophic collisions among IDPs could be a dominant mechanism for loosing IDPs if their particle sizes are larger than $\sim$ 200 μm (Dohnanyi 1978; Grün et al. 1985; Steel & Elford 1986). Despite the simplified

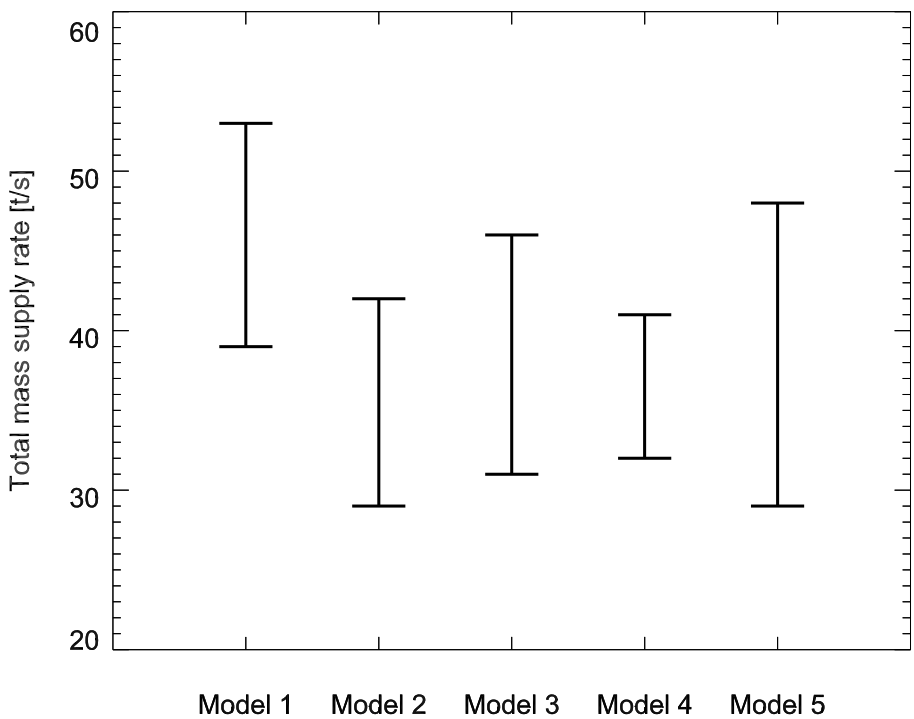

Figure 3.6. Total mass supply rate for models with validated initial parameters. The resulting values from all different densities are included.

models in these references where IDPs revolve in the fixed circular orbits, their estimated values have been considered in recent dynamical studies for cometary dust particles with eccentric orbits (Wiegert et al. 2009; Nesvorný et al. 2011; Pokorný et al. 2014). More recently, Soja et al. (2016) derived the collisional lifetime for particles on various fixed eccentric orbits, and the lifetime was comparable with P-R lifetime for 100 μm particles. On another front, the orbital distribution of helion meteors favors a collisional lifetime longer than Grün et al. (1985)'s estimate (Nesvorný et al. 2011). From the observational aspect, Jenniskens et al. (2016) discovered 7-mm meteorites delivered to the Earth which have low eccentric orbits, suggesting that such dust particles were migrated via P–R drag before collisional breakup. To sum up these bibliographic background, it is required to calculate the collisional lifetime in a more realistic manner, where the orbits of IDPs evolve under planetary perturbations and P–R drag.

As mentioned in subsection 3.3.1, most dust particles from JFCs are kicked out to orbits with large a values and stay for a long time in the outer solar system. Frequently, even the particles eventually fall to the Sun, are kicked out to orbits with large a values and spent most of their lifetimes in such orbits. Furthermore, the eccentricity of their orbits does not decrease as in the situation with no planets. When we consider these factors along with the dynamical lifetimes of dust particles that are shorter than the P–R timescale, we can expect a lower probability of mutual collision in the IDP cloud complex. In this paper, we quantitatively treated the mutual collisions and discussed whether the impact effect is significant. We did not consider the impact velocity and consequence of collision, but calculated the probability of collision regardless of impact velocity. We think this choice can simplify required treatments during calculation.

We calculated the volume swept by a dust particle during orbital evolution. At each epoch, we also calculated the cross-section density on the positions of the dust particle orbit as a function of particle size. By integrating the multiplication of these two values (i.e., the swept volume and the cross-section density), we derived the cross-section swept by the dust particle. By dividing the swept cross-section by the cross-section of responsible single particle (i.e., the projectile), we derived the contact probability for given epochs. We defined the contact timescale by dividing the dynamical lifetime by total contact probability, which is the integration of the contact probability over the entire dynamical lifetime. The contact timescale was calculated as a function of the smallest projectile size considered. The timescales are shown in Figure 3.2.

As we can see in Figure 3.2, mutual contact between particles with a size ratio that is larger than 1:100 (a mass ratio of one to million) will not happen in the IDP cloud complex. Because we did not concern the impact speed of these contacts, we

are not sure how large a projectile is required to break the target dust particle, but it is expected that a projectile 100 times smaller than the target will not destroy it. In addition, we do not know the projectile size that is required to break the fluffy aggregates. The values in Figure 3.2 are from the case in which fluffy aggregates have the longest dynamical lifetime and the largest size (a 3-mm diameter), the case in which particles most easily experience collision. When we consider that fluffy aggregates were fragmented by collisions with impact speeds of $\sim$ cm s^{-1} in the COSIMA detector on the *Rosetta* spacecraft (Hilchenbach et al. 2016), we think contact with a 25-μm projectile would break the 3-mm fluffy aggregates at least partially, but we are not sure about exact consequences of contact. However, in overall, we can see that fluffy aggregates will not experience mutual collisions, especially at sizes smaller than millimeters in diameter.

3.4 The relative importance of particles: source, size, and shape

We list the relative contribution to the gegenschein brightness as a function of source and size in Table 3.9, adopting the case of a compact particle model with a 1.9-g cm^{-3} density. The difference is not large for other cases. A dominant fraction ($> 90\%$) of gegenschein brightness is caused by dust particle from JFCs, the β of which is in the range of $0.057 - 0.00285$ ($10 - 200$ μm in diameter for $\rho = 1.9$ g cm^{-3}). However, when we derived the relative contributions of each source to the dust particles around the orbit of the Earth as a function of size, for the particles $\gtrsim 1$ mm, the contribution of ETC-2 dust particles is even larger than that of JFC particles, as shown in Table 3.10. Typically, dust particles ejected from 2P/Encke have lifetimes of $\sim$100 thousands years even for the largest particles, requiring $\sim$half of the lifetime to reach $a < 1$ au. Although the past activities of 2P/Encke and similar objects (i.e., ETC–2) are not well known, we found that dust ejected from 2P/Encke will be more important than dust ejected from any other comet at least for large dust particles in the inner solar system. Additionally, large dust particles ejected from AAs would have larger contribution to the IDP cloud complex at small heliocentric distances than to the dust supply rate, though further research is needed to survey the dust production rates and the occurrence of AAs. Therefore, when we observe zodiacal light, meteors in the sky, and meteorites on the surface of the Earth, there is the possibility that we are observing different types of particles for each observation.

We tabulated following values for compact particles and fluffy aggregates in Tables

Table 3.9. Relative contribution to the total gegenschein brightness

β	JFC	HTC	ETC	AA
0.057 −	12.2	0.0	0.8	0.7
0.0114 − 0.057	36.9	0.0	1.6	3.3
0.00285 − 0.011	32.6	0.0	1.0	4.0
− 0.00285	4.9	0.0	0.1	1.9

Table 3.10. Relative contribution to the number density around the Earth's orbit. Percentage calculated size by size

$\beta =$	0.114	0.057	0.0114	0.0057	0.00285	0.00114	0.00057
JFC	87.6	89.1	81.1	85.5	81.0	52.9	37.5
ETC-1	6.0	4.2	3.6	2.8	2.2	0.4	0.9
ETC-2	6.4	6.7	15.2	11.7	16.8	46.7	61.6

3.7 and 3.8: mass supply rate, contribution to the gegenschein brightness, and fractional mass around the Earth's orbit. As measured by Fulle et al. (2015) in the coma of 67P/Churyumov-Gerasimenko, the fluffy aggregates have small relative contributions at the moment of ejection. The contribution of these fluffy aggregates to the zodiacal light brightness is also small, that is, as much as $\sim$1−20 %. Therefore, in our methodology, the total mass supply rate to the IDP cloud complex does not largely change with or without fluffy aggregates. However, as shown in Table 3.8, their contribution may be significantly large in the sense of number density (or mass) near the Earth's orbit. Therefore, our results suggest that fluffy IDPs discovered in the Earth's stratosphere, which have similar fractal dimensions as the fluffy aggregates from 67P/Churyumov-Gerasimenko (Katyal et al. 2014), were possibly ejected from comets such as 67P.

3.5 Summary

In this chapter, we followed the evolution of dust particles ejected from cometary nuclei, considering different initial orbits, shapes and SFDs. According to our model, the total mass supply rate from comets to the IDP cloud complex is 29−53 tons s^{-1}. We discovered

that if we introduce fluffy aggregates, the dust SFD measured in cometary comae can be evolved into the dust SFD measured around the Earth's orbit. Even though initial fractional mass of fluffy aggregates is small at the source regions, cometary comae, these aggregates may represent a relatively large fraction of the mass around the Earth's orbit. Based on our findings above, we conjecture an initial dust SFD and mass supply rate that are different from those in Wiegert et al. (2009); Nesvorný et al. (2011) without altering their conclusions of the dominant cometary contribution to IDPs, zodiacal light brightness model and helion meteor orbital distribution.

Furthermore, we identified that large dust particles ejected from JFCs cannot be easily transferred to a small a orbit because of close encounters with Jupiter. Therefore, the contribution from ETC-2s may be high for large dust particles in small a orbits.

Finally, we directly calculated the probability of mutual collisions between dust particles in the IDP cloud complex and concluded that mutual collisions are ignorable. This collisional lifetime is figurally (a factor of 10 or less) longer than the simplified estimate by Soja et al. (2016), while the dynamical lifetime is more than an order of magnitude shorter than the collisional lifetime in Soja et al. (2016). We conjecture that Jenniskens et al. (2016)'s discovery, large meteorites on low eccentricity orbits, were possibly caused by fluffy aggregates, which have small eccentricities around the Earth's orbit, unlike the compact particles from 2P/Encke or JFCs.

Chapter 4

Conclusion

In this dissertation, we studied the origins of IDPs. In chapter 2, we provided the geometric albedo of IDPs, and together with the spectral slope from the previous studies, compared these optical properties with those of solar system minor bodies. As a result, we found that more than 90 % of cometary dust particles contribute to the IDPs cloud complex. In chapter 3, we studied the orbital and collisional evolution of cometary dust particles. As a result, we confirmed that SFD of IDPs measured around the Earth's orbit can be explained by the SFD of cometary dust particles, without any contributions from other dust sources. We think that these concurrences of these two results support a dominant fraction of cometary dust particles in IDPs.

In addition to these findings, we revealed details about the evolution of cometary dust particles which were unexplained in previous studies. We thus noticed that cometary dust particles may not experience collisional breakup during its evolution. However, large ($> 100\mu$m) dust particles ejected from JFCs are kicked out from the solar system through close encounters with Jupiter, therefore not migrated into the inner solar system despite the negligible mutual collisions.

Meanwhile, there are questions raised by this work. From the study of IDPs optical properties, we discovered that spectra of IDPs are similar with chondritic porous micrometeorites which have fluffy structures. Our dynamical work involving SFD of IDPs also favors the existence of fluffy cometary dust particles. This dissertation requires further investigation about fluffy aggregates. The first question is whether the chondritic porous micrometeorites were originally fluffy aggregates at cometary comae. The second question is the optical properties of cometary fluffy aggregates, which we had to assume in chapter 3. Currently, there are no measurements about the optical properties or structure of cometary fluffy aggregates. Future space missions may supply information about

cometary fluffy particles. We hope this dissertation will help further studies about fluffy aggregates, like theoretical structure modelling, space weathering on the aggregates, and dynamical evolution of aggregates.

This research exposed limits in its input data and methodology. We measured the albedo of IDPs at the anti-solar direction, and used spectral gradient of IDPs measured at different direction (phases angles between 90°–180°). Further investigations are required, such as spectroscopic observation of the zodiacal light in various viewing geometry. If there are such data, this research may yield more accurate and more precise results using the same methods.

We explained IDPs SFD with cometary dust particles only. However, we cannot rule out possibility that IDPs are a mixture of dust particles from different source populations. We did not pursue this part deeply in this dissertation, although dust particles from AAs experienced orbital evolutionary track very different with those from JFCs. Especially, dust particles from AAs usually have a low velocity relative to the Earth when they approach the Earth. Therefore, even though their overall contribution to the IDPs cloud is not high, they may cause interesting consequences in the near Earth region. We plan to investigate this question as our next subject.

We suggested other meaningful values which may be used in many different kind of researches. We directly derived the albedo of IDPs as 0.06 ± 0.01, and dust ejection from comets as 30–50 tons s^{-1}. This values will be helpful to other researchers.

Bibliography

Abell, P. A., Fernández, Y. R., Pravec, P., et al. 2005, Icarus, 179, 174

Agarwal, J., A'Hearn, M. F., Vincent, J.-B., et al. 2016, MNRAS, 462, S78

A'Hearn, M. F., Campins, H., Schleicher, D. G., & Millis, R. L. 1989, ApJ, 347, 1155

Altobelli, N., Dikarev, V., Kempf, S., et al. 2007, Journal of Geophysical Research (Space Physics), 112, A07105

Belheouane, S., Zaslavsky, A., Meyer-Vernet, N., et al. 2012, Sol. Phys., 281, 501

Bentley, M. S., Schmied, R., Mannel, T., et al. 2016, Nature, 537, 73

Binzel, R. P., Rivkin, A. S., Stuart, J. S., et al. 2004, Icarus, 170, 259

Bloxam, K., & Campbell-Brown, M. 2017, Planet. Space Sci., 143, 28

Boehnhardt, H., Tozzi, G. P., Bagnulo, S., et al. 2008, A&A, 489, 1337

Bradley, J. P. 2003, Treatise on Geochemistry, 1, 689

Bradley, J. P., Keller, L. P., Brownlee, D. E., & Thomas, K. L. 1996, Meteoritics and Planetary Science, 31, 394

Brownlee, D. E. 1985, Annual Review of Earth and Planetary Sciences, 13, 147

Buffington, A., Bisi, M. M., Clover, J. M., et al. 2009, Icarus, 203, 124

Burns, J. A., Lamy, P. L., & Soter, S. 1979, Icarus, 40, 1

—. 2014, Icarus, 232, 263

Bus, S. J. 1999, PhD thesis, Massachusetts Institute of Technology

Bus, S. J., & Binzel, R. P. 2002a, Icarus, 158, 106

—. 2002b, Icarus, 158, 146

Busemann, H., Nguyen, A. N., Cody, G. D., et al. 2009, Earth and Planetary Science Letters, 288, 44

Campins, H., A'Hearn, M. F., & McFadden, L.-A. 1987, ApJ, 316, 847

Campins, H., & Fernández, Y. 2002, Earth Moon and Planets, 89, 117

Campins, H., Licandro, J., Pinilla-Alonso, N., et al. 2007, AJ, 134, 1626

Campins, H., Ziffer, J., Licandro, J., et al. 2006, AJ, 132, 1346

Chambers, J. E. 1999, MNRAS, 304, 793

Della Corte, V., Rotundi, A., Fulle, M., et al. 2015, A&A, 583, A13

—. 2016, MNRAS, 462, S210

DeMeo, F. E., Binzel, R. P., Carry, B., Polishook, D., & Moskovitz, N. A. 2014, Icarus, 229, 392

DeMeo, F. E., & Carry, B. 2013, Icarus, 226, 723

Dermott, S. F., Grogan, K., Gustafson, B. A. S., et al. 1996, in Astronomical Society of the Pacific Conference Series, Vol. 104, IAU Colloq. 150: Physics, Chemistry, and Dynamics of Interplanetary Dust, ed. B. A. S. Gustafson & M. S. Hanner, 143

Dermott, S. F., Jayaraman, S., Xu, Y. L., Gustafson, B. Å. S., & Liou, J. C. 1994, Nature, 369, 719

Dermott, S. F., Nicholson, P. D., Burns, J. A., & Houck, J. R. 1984, Nature, 312, 505

Dikarev, V., & Grün, E. 2002, A&A, 383, 302

Dikarev, V., Grün, E., Baggaley, J., et al. 2005, Advances in Space Research, 35, 1282

Dikarev, V., Grün, E., Landgraf, M., Baggaley, W. J., & Galligan, D. P. 2001, in ESA Special Publication, Vol. 495, Meteoroids 2001 Conference, ed. B. Warmbein, 609–615

Divine, N. 1993, J. Geophys. Res., 98, 17029

Dohnanyi, J. S. 1969, J. Geophys. Res., 74, 2531

—. 1978, Particle dynamics, ed. J. A. M. McDonnell, 527–605

Draine, B. T. 2003, ApJ, 598, 1017

Dumont, R., & Levasseur-Regourd, A.-C. 1988, A&A, 191, 154

Durda, D. D., & Dermott, S. F. 1997, Icarus, 130, 140

Engrand, C., & Maurette, M. 1998, Meteoritics and Planetary Science, 33, 565

Everhart, E. 1985, in Dynamics of Comets: Their Origin and Evolution, Proceedings of IAU Colloq. 83, held in Rome, Italy, June 11-15, 1984. Edited by Andrea Carusi and Giovanni B. Valsecchi. Dordrecht: Reidel, Astrophysics and Space Science Library. Volume 115, 1985, p.185, ed. A. Carusi & G. B. Valsecchi, 185

Farley, K. A., Vokrouhlický, D., Bottke, W. F., & Nesvorný, D. 2006, Nature, 439, 295

Fechtig, H., Leinert, C., & Berg, O. E. 2001, Interplanetary Dust, ed. E. Grun, B. A. S. Gustafson, S. Dermott, & H. Fechtig (Springer Berlin Heidelberg), 1–56

Fernández, Y. R. 2009, Planetary and Space Science, 57, 1218

Fernández, Y. R., Campins, H., Kassis, M., et al. 2006, AJ, 132, 1354

Fernández, Y. R., Lisse, C. M., Ulrich Käufl, H., et al. 2000, Icarus, 147, 145

Fernández, Y. R., Kelley, M. S., Lamy, P. L., et al. 2013, Icarus, 226, 1138

Fixsen, D. J., & Mather, J. C. 2002, ApJ, 581, 817

Fulle, M., Colangeli, L., Mennella, V., Rotundi, A., & Bussoletti, E. 1995, A&A, 304, 622

Fulle, M., Della Corte, V., Rotundi, A., et al. 2015, ApJ, 802, L12

Fulle, M., Marzari, F., Della Corte, V., et al. 2016a, ApJ, 821, 19

Fulle, M., Della Corte, V., Rotundi, A., et al. 2016b, MNRAS, 462, S132

Gor'kavyi, N. N., Ozernoy, L. M., & Mather, J. C. 1997, ApJ, 474, 496

Green, S. F., McDonnell, J. A. M., McBride, N., et al. 2004, Journal of Geophysical Research (Planets), 109, E12S04

Green, S. F., McBride, N., Colwell, M. T. S. H., et al. 2007, Dust in Planetary Systems, 643, 35

Grün, E., Zook, H. A., Fechtig, H., & Giese, R. H. 1985, Icarus, 62, 244

Gueymard, C. A. 2004, Solar Energy, 76, 423

Gustafson, B. A. S. 1994, Annual Review of Earth and Planetary Sciences, 22, 553

Hahn, J. M., Zook, H. A., Cooper, B., & Sunkara, B. 2002, Icarus, 158, 360

Hanayama, H., Ishiguro, M., Watanabe, J.-I., et al. 2012, PASJ, 64, doi:10.1093/pasj/64.6.134

Hanner, M. S. 1980, Icarus, 43, 373

Hanner, M. S., Giese, R. H., Weiss, K., & Zerull, R. 1981, A&A, 104, 42

Hilchenbach, M., Kissel, J., Langevin, Y., et al. 2016, ApJ, 816, L32

Hiroi, T., & Sasaki, S. 2012, LPI Contributions, 1667, 6109

Ipatov, S. I., Kutyrev, A. S., Madsen, G. J., et al. 2008, Icarus, 194, 769

Ishiguro, M., Nakamura, R., Fujii, Y., et al. 1999, ApJ, 511, 432

Ishiguro, M., Sarugaku, Y., Ueno, M., et al. 2007, Icarus, 189, 169

Ishiguro, M., Usui, F., Sarugaku, Y., & Ueno, M. 2009, Icarus, 203, 560

Ishiguro, M., Yang, H., Usui, F., et al. 2013, ApJ, 767, 75

Ishiguro, M., Ueno, M., Usui, F., et al. 2003, in Proc. SPIE, Vol. 4842, Specialized Optical Developments in Astronomy, ed. E. Atad-Ettedgui & S. D'Odorico, 366–374

Ishiguro, M., Hanayama, H., Hasegawa, S., et al. 2011, The Astrophysical Journal Letters, 741, L24

Ishiguro, M., Jewitt, D., Hanayama, H., et al. 2014, The Astrophysical Journal, 787, 55

Ishiguro, M., Sarugaku, Y., Kuroda, D., et al. 2016a, The Astrophysical Journal, 817, 77

Ishiguro, M., Kuroda, D., Hanayama, H., et al. 2016b, The Astronomical Journal, 152, 169

Jenniskens, P., Nénon, Q., Gural, P. S., et al. 2016, Icarus, 266, 384

Jeong, J. 2014, Master's thesis, Seoul National University

Jewitt, D., Agarwal, J., Li, J., et al. 2017, The Astronomical Journal, 153, 223

Jewitt, D., Hsieh, H., & Agarwal, J. 2015, The Active Asteroids, ed. P. Michel, F. E. DeMeo, & W. F. Bottke, 221–241

Jewitt, D., Ishiguro, M., & Agarwal, J. 2013, ApJ, 764, L5

Jewitt, D., & Luu, J. 1989, AJ, 97, 1766

Jewitt, D., Mutchler, M., Weaver, H., et al. 2016, The Astrophysical Journal Letters, 829, L8

Jorda, L., Lamy, P., Groussin, O., et al. 2000, in ESA Special Publication, Vol. 455, ISO Beyond Point Sources: Studies of Extended Infrared Emission, ed. R. J. Laureijs, K. Leech, & M. F. Kessler, 61

Katyal, N., Banerjee, V., & Puri, S. 2014, Journal of Quantitative Spectroscopy and Radiative Transfer, 146, 290 , electromagnetic and Light Scattering by Nonspherical Particles XIV

Kawara, K., Matsuoka, Y., Sano, K., et al. 2017, PASJ, 69, 31

Keller, H. U., Delamere, W. A., Reitsema, H. J., Huebner, W. F., & Schmidt, H. U. 1987, A&A, 187, 807

Kelley, M. S., Wooden, D. H., Tubiana, C., et al. 2009, AJ, 137, 4633

Kelsall, T., Weiland, J. L., Franz, B. A., et al. 1998, ApJ, 508, 44

Kim, Y., Ishiguro, M., Michikami, T., & Nakamura, A. M. 2017, The Astronomical Journal, 153, 228

Klačka, J., Petržala, J., Pástor, P., & Kómar, L. 2014, Icarus, 232, 249

Kondo, T., Ishihara, D., Kaneda, H., et al. 2016, AJ, 151, 71

Kortenkamp, S. J. 2013, Icarus, 226, 1550

Krüger, H., Strub, P., Grün, E., & Sterken, V. J. 2015, ApJ, 812, 139

Krüger, H., Grün, E., Hamilton, D. P., et al. 1998, Planet. Space Sci., 47, 85

Krüger, H., Grün, E., Graps, A., et al. 2001, Planet. Space Sci., 49, 1285

Krüger, H., Altobelli, N., Anweiler, B., et al. 2006, Planet. Space Sci., 54, 932

Kuchner, M. J., & Stark, C. C. 2010, AJ, 140, 1007

Kwon, S. M., Hong, S. S., & Weinberg, J. L. 2004, New Astronomy, 10, 91

Lamy, P. L., Toth, I., Groussin, O., et al. 2008, A&A, 489, 777

Lamy, P. L., Toth, I., Weaver, H. A., et al. 2006, A&A, 458, 669

Leinert, C., Bowyer, S., Haikala, L. K., et al. 1998, A&AS, 127, 1

Levison, H. F. 1996, in Astronomical Society of the Pacific Conference Series, Vol. 107, Completing the Inventory of the Solar System, ed. T. Rettig & J. M. Hahn, 173–191

Levison, H. F., & Duncan, M. J. 1994, Icarus, 108, 18

—. 1997, Icarus, 127, 13

Li, J.-Y., A'Hearn, M. F., Belton, M. J. S., et al. 2007, Icarus, 187, 41

Li, J.-Y., Besse, S., A'Hearn, M. F., et al. 2013, Icarus, 222, 559

Loehle, S., Zander, F., Hermann, T., et al. 2017, ApJ, 837, 112

Low, F. J., Young, E., Beintema, D. A., et al. 1984, ApJ, 278, L19

Lumme, K., & Bowell, E. 1985, Icarus, 62, 54

Luu, J., & Jewitt, D. 1990, Icarus, 86, 69

Luu, J. X. 1993, Icarus, 104, 138

Mann, I. 2010, ARA&A, 48, 173

Mann, I., & Czechowski, A. 2005, ApJ, 621, L73

Mann, I., Köhler, M., Kimura, H., Cechowski, A., & Minato, T. 2006, A&A Rev., 13, 159

Mann, I., Meyer-Vernet, N., & Czechowski, A. 2014, Phys. Rep., 536, 1

Mannel, T., Bentley, M. S., Schmied, R., et al. 2016, MNRAS, 462, S304

Matsumoto, T., Kawada, M., Murakami, H., et al. 1996, PASJ, 48, L47

Matsuura, S., Matsumoto, T., Matsuhara, H., & Noda, M. 1995, Icarus, 115, 199

Mazzotta Epifani, E., Palumbo, P., & Colangeli, L. 2009, A&A, 508, 1031

McAdam, M. M., Sunshine, J. M., Howard, K. T., & McCoy, T. M. 2015, Icarus, 245, 320

Melita, M. D., & Licandro, J. 2012, A&A, 539, A144

Merouane, S., Zaprudin, B., Stenzel, O., et al. 2016, A&A, 596, A87

Messenger, S. 2002, Meteoritics and Planetary Science, 37, 1491

Milani, A., & Knezevic, Z. 1990, Celestial Mechanics and Dynamical Astronomy, 49, 347

—. 1994, Icarus, 107, 219

Millis, R. L., A'Hearn, M. F., & Campins, H. 1988, ApJ, 324, 1194

Moreno, F., Licandro, J., Álvarez-Iglesias, C., Cabrera-Lavers, A., & Pozuelos, F. 2014, The Astrophysical Journal, 781, 118

Moroz, L., Baratta, G., Strazzulla, G., et al. 2004, Icarus, 170, 214

Mothé-Diniz, T., Carvano, J. M. á., & Lazzaro, D. 2003, Icarus, 162, 10

Mukai, T., Ishimoto, H., Kozasa, T., Blum, J., & Greenberg, J. M. 1992, A&A, 262, 315

Murray, C. D., & Dermott, S. F. 1999, Solar system dynamics

Nesvorný, D., Bottke, W. F., Vokrouhlický, D., et al. 2008, ApJ, 679, L143

Nesvorný, D., Janches, D., Vokrouhlický, D., et al. 2011, ApJ, 743, 129

Nesvorný, D., Jenniskens, P., Levison, H. F., et al. 2010, ApJ, 713, 816

Nesvorný, D., Vokrouhlický, D., Bottke, W. F., & Sykes, M. 2006, Icarus, 181, 107

Noguchi, T., Ohashi, N., Tsujimoto, S., et al. 2015, Earth and Planetary Science Letters, 410, 1

Ootsubo, T., Ueno, M., Ishiguro, M., et al. 2009, in Astronomical Society of the Pacific Conference Series, Vol. 418, AKARI, a Light to Illuminate the Misty Universe, ed. T. Onaka, G. J. White, T. Nakagawa, & I. Yamamura, 395

Opik, E. J. 1951, Proc. R. Irish Acad. Sect. A, vol. 54, p. 165-199 (1951)., 54, 165

Pajola, M., Lazzarin, M., Dalle Ore, C. M., et al. 2013, ApJ, 777, 127

Pajola, M., Lazzarin, M., Bertini, I., et al. 2014, Memorie della Societa Astronomica Italiana Supplementi, 26, 67

Plane, J. M. C., Flynn, G. J., Määttänen, A., et al. 2018, Space Sci. Rev., 214, 23

Pokorný, P., Vokrouhlický, D., Nesvorný, D., Campbell-Brown, M., & Brown, P. 2014, ApJ, 789, 25

Poppe, A., James, D., Jacobsmeyer, B., & Horányi, M. 2010, Geophys. Res. Lett., 37, L11101

Poppe, A. R. 2016, Icarus, 264, 369

Poppe, A. R., & Horányi, M. 2012, Geophys. Res. Lett., 39, 15104

Pyo, J., Ueno, M., Kwon, S. M., et al. 2010, A&A, 523, A53

Reach, W. T., Morris, P., Boulanger, F., & Okumura, K. 2003, Icarus, 164, 384

Rotundi, A., Sierks, H., Della Corte, V., et al. 2015, Science, 347, aaa3905

Rowan-Robinson, M., & May, B. 2013, MNRAS, 429, 2894

Sagdeev, R. Z., Blamont, J., Galeev, A. A., et al. 1986, Nature, 321, 259

Sandford, S. A., & Walker, R. M. 1985, ApJ, 291, 838

Shestopalov, D. I., Golubeva, L. F., & Cloutis, E. A. 2013, Icarus, 225, 781

Skorov, Y., Reshetnyk, V., Lacerda, P., Hartogh, P., & Blum, J. 2016, MNRAS, 461, 3410

Snodgrass, C., Fitzsimmons, A., Lowry, S. C., & Weissman, P. 2011, MNRAS, 414, 458

Soja, R. H., Schwarzkopf, G. J., Sommer, M., et al. 2016, in International Meteor Conference Egmond, the Netherlands, 2-5 June 2016, ed. A. Roggemans & P. Roggemans, 284–286

Stansberry, J., Grundy, W., Brown, M., et al. 2008, Physical Properties of Kuiper Belt and Centaur Objects: Constraints from the Spitzer Space Telescope, ed. M. A. Barucci, H. Boehnhardt, D. P. Cruikshank, A. Morbidelli, & R. Dotson, 161–179

Steel, D. I., & Elford, W. G. 1986, MNRAS, 218, 185

Sterken, V. J., Strub, P., Krüger, H., von Steiger, R., & Frisch, P. 2015, ApJ, 812, 141

Sykes, M. V., & Greenberg, R. 1986, Icarus, 65, 51

Tancredi, G., Fernández, J. A., Rickman, H., & Licandro, J. 2006, Icarus, 182, 527

Thomas, N., & Keller, H. U. 1989, A&A, 213, 487

Toller, G. N. 1981, PhD thesis, State Univ. of New York, Stony Brook (USA)

Tsumura, K., Matsumoto, T., Matsuura, S., et al. 2013, PASJ, 65, 119

Tsumura, K., Battle, J., Bock, J., et al. 2010, ApJ, 719, 394

Tubiana, C., Barrera, L., Drahus, M., & Boehnhardt, H. 2008, A&A, 490, 377

Ueda, T., Kobayashi, H., Takeuchi, T., et al. 2017, AJ, 153, 232

Usui, F., Kasuga, T., Hasegawa, S., et al. 2013, ApJ, 762, 56

Usui, F., Kuroda, D., Müller, T. G., et al. 2011, PASJ, 63, 1117

Vaubaillon, J. J., & Reach, W. T. 2010, AJ, 139, 1491

Vitense, C., Krivov, A. V., Kobayashi, H., & Löhne, T. 2012, A&A, 540, A30

Vitense, C., Krivov, A. V., & Löhne, T. 2014, AJ, 147, 154

Wiegert, P., Vaubaillon, J., & Campbell-Brown, M. 2009, Icarus, 201, 295

Yamamoto, S., & Mukai, T. 1998, Earth, Planets, and Space, 50, 531

Yang, H. 2012, Master's thesis, Seoul National University

Yang, H., & Ishiguro, M. 2015, ApJ, 813, 87

—. 2018, ApJ, accepted

초록

본 논문에서는 행성간 티끌 (IDP)의 기원과 진화를 연구하였다. IDP가 행성간 공간에 존재하기 위해서는 태양계의 어딘가에서부터 현재, 또는 최근에 IDP가 계속 공급되었어야만 한다. 혜성, 소행성 등이 IDP의 기원으로 제안되고 있으나, 과연 전체 IDP 공급에 대한 이들의 비중이 얼마나 될지는 연구 방법에 따라 다른 답이 나오고 있다. 본 논문에서는 기존의 연구에서 시도되지 않았던 새로운 방법으로 독립적인 결론을 도출하였다. 우리는 태양 정반대 방향에서 황도광의 광학영역 밝기를 측정하였고, 이로부터 IDP의 평균 반사도를 0.06 ± 0.01로 도출하였다. 우리는 이 반사도 값과 황도광 연속반사 스펙트럼의 기울기를 각종 태양계 천체의 값과 비교하였다. 베이즈 추론을 통해 도출된 결과에 따르면, 약 $> 90\%$ 이상의 IDP가 혜성 (또는 혜성과 같은 스펙트럼을 가지는 D–형 소행성) 에서 기인하였을 때 황도광의 광학 특성이 잘 설명된다.

그 후, 우리는 혜성에서 방출된 티끌의 궤도 진화를 수치적으로 연구하였다. 행성의 섭동과 태양 복사가 언제나 티끌에 영향을 주고 있는 상황에서, 티끌의 조밀하지 않은 구조 및 티끌간의 상호 충돌을 고려하였다. 우리는 혜성의 코마에서 (1P/Halley, 67P/Churyumov-Gerasimenko, 73P/Schwassmann-Wachmann 3, and 81P/Wild 2) 측정된 티끌의 크기도수 분포로부터 지구 궤도에서 측정된 IDP의 크기도수분포를 재현하는 데 성공하였다.

이 외에 본 연구에서 새로 밝혀낸 사실은 다음과 같다. (1) IDP의 스펙트럼은 지구의 성층권에서 수집되는 "chondritic porous" 미소유성체와 유사하다. (2) 혜성에서 방출된 티끌들은 상호간의 충돌을 겪지 않는다. (3) 목성족 혜성에서 방출된 티끌은 크기가 100 μm 보다 클 경우 대부분 목성과의 근접 조우로 인하여 태양계 바깥으로 튕겨 나가게 된다. (4) 목성족 및 엔케형혜성에서 IDP 구름으로 공급되는 티끌의 총량은 대략 초당 30–50 톤에 달한다.